Eidgenössische Technische Hochschule Zürich
Swiss Federal Institute of Technology Zurich

Kondo Physics with Matrix Product States

Master's Thesis

Stefan H. Sack

September 30, 2018

Prof. Dr. Oded Zilberberg
Michael Ferguson

Institute for Theoretical Physics, ETH Zürich

Abstract

In this work we present a Matrix Product State based approach to Kondo physics in Quantum Impurity systems. We use the Density Matrix Renormalization Group to calculate the ground state of the Anderson Impurity model and a quantum dot coupled to an electronic cavity. Occupation and correlation features are analyzed to give information about the entanglement properties of both systems. Additionally, we develop a Quantum Information technique that allows to specifically target Kondo physics. We discover a surprising phase transition between non-Kondo and Kondo physics in the bond dimension of the Matrix Product States and confirm a singlet-triplet formation of the electrons in the quantum dot and electronic cavity.

Acknowledgements

Foremost, I would like to express my gratitude to my thesis advisors Prof. Dr. Oded Zilberberg and Michael Ferguson for their continuous support, for their immense knowledge and for always having an open door for me. Prof. Dr. Oded Zilberberg helped me to keep the big picture in mind and taught me an intuitive and interconnected understanding of physics. Michael Ferguson confronted me with the devil in the details and showed me how to tame it. I have learned many valuable lessons and I am grateful for the experience.

I want to thank my colleagues and office mates Christoph, Yuto, Filippo, Christian and Jonas, lunch and coffee would have been half as fun without them. Especially the countless discussions about physics with Christoph and Yuto provided me with new insights and perspectives that kept me motivated.

I thank my grandad and former biology teacher for sparking my interest in the natural sciences and promoting my curiosity, without them I would not be where I am today.

Lastly, I want to thank my parents, they gave me the opportunity to pursue my dream and follow my passion. They taught me to never give up and made all of this possible, I owe it all to them.

Contents

Contents **iii**

1 Introduction **1**
- 1.1 Model . . . 3
  - 1.1.1 Quantum Computers . . . 3
  - 1.1.2 Quantum Dots . . . 5
  - 1.1.3 Quantum Dot coupled to an Electronic Cavity . . . 7
  - 1.1.4 The Anderson Impurity Model . . . 9
  - 1.1.5 The Kondo Problem . . . 10
  - 1.1.6 Schrieffer Wolff transformation . . . 12
  - 1.1.7 Kondo Resonance and Kondo Singlet . . . 13

2 Methods **15**
- 2.1 Numerical Renormalization Group . . . 15
  - 2.1.1 Logarithmic discretization . . . 16
  - 2.1.2 Conversion to a hopping Hamiltonian . . . 19
  - 2.1.3 Numerical Renormalization Group in its classical formulation . . . 20
- 2.2 Matrix Product States . . . 22
  - 2.2.1 Singular Value Decomposition . . . 23
  - 2.2.2 Area law . . . 24
  - 2.2.3 Graphical representation . . . 25
  - 2.2.4 Quantum Impurity Matrix Product Operator . . . 27
- 2.3 Density Matrix Renormalization Group . . . 28
  - 2.3.1 Numerical Renormalization Group in Matrix Product State language . . . 30
- 2.4 Quantum Information Approach . . . 32

3 Results **35**
- 3.1 Occupation Properties . . . 35

3.1.1 Correlation Properties 40
3.2 Quantum Information Approach 42
3.2.1 Purity flow 42
3.2.2 Kondo Singlet formation in the Anderson Impurity model 44
3.2.3 Purity of a Quantum Dot coupled to an Electronic Cavity 48

4 Conclusion and Outlook 51

A Fermionic operators 53

B Purity of a Singlet state 55

C Numerical Renormalization Group 57
C.0.1 Renormalization Group Flow 57
C.0.2 No spectral function 58

D Kernel Polynomial Method 61
D.0.1 Rescaling the spectrum 62
D.0.2 Chebychev expansion 63
D.1 No Spectral function 63

Bibliography 65

Chapter 1

Introduction

> A physicist is just an atom's way of looking at itself.
>
> *Niels Bohr*

We humans are very lucky creatures, we carry the most complex structure of the universe right between our ears. Our brains allow us to seemingly perform unthinkable calculations within an instant, they are capable of the extraordinary, yet absurdly limited in some regards. From the abacus to today's supercomputers, it is this conjecture that led to the development of machines that are capable of computations, more efficiently, faster and sometimes even incomprehensible for humans. Computers may seem like magic for the laymen. Yet, at its core they work on a rather simple principle, zero or one, up or down, every operation on a computer is based on bits, the fundamental unit of computation. This elegant simplicity allows for any thinkable computation, though at the same time hinders us to go beyond, some computations would take millions of years and we dare to make a start. This limitation led us to take the next step, the age of quantum computing has begun! A quantum computer, unlike a classical computer, works with a quantum mechanical superposition of zeros and ones at the same time [1]. The quantum realms are governed by equations that allow things to be multiple things at once which allows quantum computers to perform computations that were previously deemed impossible. We are still a long way from building a quantum computer with more than a few quantum bits, but once we are there, humanity will not just experience a small step forward but rather a quantum leap.

With this work we want to add a tiny piece of knowledge towards the realization of such quantum computers, particularly we are concerned with the physical realization of quantum bits, called qubits. One such promising realization of this technical challenge is given by so called quantum dots. These quantum dots [2] are fascinating things, since they are very similar to atoms but on a mesoscopic scale, thus giving raise to the name artificial atoms. Quantum dots are realized by trapping a small number of electrons in a metal inside of a potential well by applying an appropriate electric field. The electrons repel each other via the Coulomb force, thus energetically separating them. The effective remaining handful of energy levels can be occupied with electrons that can jump between the levels, just like in a real atom. The goal is thus to isolate a single electron and use its spin as a qubit. The status of current experiments on the matter is reported in Ref. [3, 4, 5]. Though, our research is not only concerned with quantum computers, quantum dots give experimentalists the possibility to specifically target the underlying mechanics of fascinating quantum many-body phenomena such as the Kondo effect [6]. This led to a renaissance in theoretical research on the matter and gives rise to new insights on an age old problem.

Promising experimental results led experimentalists to take the next step. The pressing question is how can quantum dots be coupled to each other? To build a quantum computer we need the qubits to collectively act as quantum mechanical objects by entangling them with each other. Entanglement is a counterintuitive quantum mechanical property that connects two spatially separated objects in the sense that manipulating one object instantaneously determines the property of the other object. Even Albert Einstein expressed his discomfort with this strange property by calling it *spooky action at a distance* [7].

Nevertheless, quantum mechanics is the most precisely studied theory of mankind and has stood the test of time since its first introduction by Heisenberg [8] and Schrödinger [9] in the 1920s. Theory and experiment agree up to staggering precision, a notable example is given by the fine-structure constant with an uncertainty of 0.17×10^{-11} [10].

One promising idea of entangling quantum dots is with electronic cavities. When a wave is spatially confined it will form a standing wave, just like a guitar string. An electronic cavity spatially confines electron waves in the metal and introduces distinct energy levels that can be occupied by electrons, though Coulomb interaction between them can be neglected because they are sufficiently spatially separated, the details will be discussed in the next chapter.

The quantum dot coupled to an electronic cavity has undergone some experimental [11, 12] and theoretical [13, 14] exploration. In this thesis we start our investigation to gain further insight into the physical properties of the setup. This thesis is split into three parts.

The first part comprises the motivation and introduction of our models. In particular, we will discuss the Anderson Impurity model and the associated quantum many-body phenomena known as the Kondo singlet formation [6, 15] as well as the quantum dot coupled to an electronic cavity.

In the second chapter we introduce the numerical tools that were developed to tame the complexity of quantum mechanics. We show that Matrix Product States can be used to efficiently calculate ground states [16] and use them to analyze the occupation and correlation properties of our models. In addition, we present a Quantum Information approach that specifically targets Kondo physics .

In the third part of the thesis we will discuss the numerical results that where obtained by aforementioned methods. We reveal an interesting novel phase transition between non-Kondo and Kondo physics in the Anderson Impurity model and show that the dot and electronic cavity electrons form a singlet-triplet state.

Our aim with this thesis is not to provide a thorough explanation of the experimental observations but rather to explore the theoretical properties of entanglement between the dot, electronic cavity and the environment. Our work can thus be understood as a proof of principle, however we have paved the way for future work to thoroughly explore a parameter regime that is geared towards the experiments.

Finally, the conclusion will comprise a summary of our obtained results, their implications and an outlook for future work. The Appendix additionally encloses a discussion of the Numerical Renormalization Group [17, 18] and the Kernel Polynomial Method [19, 20].

1.1 Model

In this chapter of the thesis we will start off by setting the stage for our models of interest. The emphasis is put on an intuitive understanding rather than mathematical details which can be found in the extensive literature [6, 13, 17, 21, 22]. This chapter of the thesis will not include any novel results of our work.

1.1.1 Quantum Computers

In the 21th century our lives are dominated by computers. They are everywhere and have become part of our way of life. They are a prime example of how concepts developed in theoretical physics have diffused over to the engineering domain and fundamentally impacted society. Quantum mechanics is at the core of transistors and gates, the fundamental building blocks of modern day computers, and it might thus seem like computers are fundamentally quantum machines. Surprisingly, this is not the case and computers actually operate on simple, classical units of either on or off. Current either flows or it does not, capacitors are either charged or not and the magnetization in the hard drive in a computer points either up or down. Everything is broken down in either 1 or 0. The limitations of this representation become clear, once someone tries to simulate a quantum mechanical system.

Quantum mechanics tells us that things can be in a superposition of possibilities, randomly revealing one such realization once we perform a measurement. In order to store all of these possibilities or perform simulations of said quantum systems, an exponential number of coefficients is needed. To illustrate this, let us take a look at a simple system of two spin $\frac{1}{2}$ particles. Each spin can either be $\uparrow$ or $\downarrow$. This allows for the following combinations: $\{\uparrow\uparrow, \uparrow\downarrow, \downarrow\uparrow, \downarrow\downarrow\}$. Each possibility is associated with a probability, we thus have 4 probabilities or more generally 2^N probabilities for N particles. Due to the exponential scaling, it is thus an impossible task to simulate any quantum mechanical system that has a macroscopic number of degrees of freedom. The root of this problem is that the rules of quantum mechanics tell us that a system reveals itself in one specific state upon measurement with a certain probability which we try to store classically. Though in reality this probability is only revealed after performing a number of measurements, one measurement on its own only reveals a certain state, without any probability associated to it. To efficiently simulate a quantum mechanical system, we have to circuit this exponentially scaling translation between quantum mechanics and classical logic, we want to study quantum mechanics with an inherently quantum mechanical system.

A quantum computer is a computer whose fundamental units of computation are quantum mechanical, called qubits rater than the classical bits. This idea was first laid out by Richard Feynman [1]. A qubit is a quantum mechanical state that is in a superposition of the classical logical units 1 and 0,

$$|\psi\rangle = \alpha\,|1\rangle + \beta\,|0\rangle\,, \tag{1.1}$$

where $|\alpha|^2$ and $|\beta|^2$ are the associated probabilities. Using qubits as the fundamental logical building blocks of computers, allows to perform calculations that are classically almost impossible to do. This can be understood as a consequence of the quantum mechanical superposition that allows to perform multiple logical operations simultaneously. Notable examples of applications are in the field of cryptography [23] and simulating quantum many-body systems [24].

1.1.2 Quantum Dots

Building a quantum computer is a technologically challenging endeavour, one of the fundamental challenges is the scalable realization and manipulation of qubits. One such promising realization that is currently experimentally investigated, is to spatially confine electrons in ultra clean metals by applying an appropriate potential well. A doped semiconductor is placed on top of a non-conducting material. The doping of the top layer and the chemical potential of the bottom layer are balanced such that the electrons form a 2D electron gas (2DEG) at the interface, see Ref. [25] for a detailed discussion. By applying a voltage between gates placed on top of the top layer, a potential well is created in the 2DEG at the interface, Fig. 1.1 shows a schematic sketch of the setup.

The potential well is tuned such that only a few discrete energy levels are inside the well, while energies above the Fermi energy ε_F form a continuum. The physically relevant energy levels are the ones that are populated by electrons. The potential can be tuned such that only one level is populated. A second added electron will populate the same energy level with opposite spin direction, though due to the spatial confinement the electrons will exhibit a Coulomb repulsion. Adding an electron thus increases the total energy by the Coulomb integral.

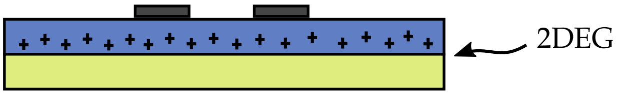

Figure 1.1: The 2D electron gas (2DEG) is generated by placing a doped semiconductor on a non-conducting material. The chemical potentials are balanced such that the electrons form a 2DEG at the interface between the two materials. See Ref. 1.1 for details. Top gates generate a potential well, sketched in Fig. 1.2

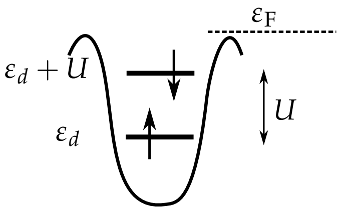

Figure 1.2: Potential well with two trapped electrons separated energetically by the Coulomb repulsion U. The Fermi surface is indicated by the dashed line.

Fig. 1.2 shows how we can picture this situation, where ε_d is the kinetic energy of the electron, U is the Coulomb repulsion, and ε_F is the Fermi energy. The Hamiltonian of this system in second quantization is given by

$$H^{\text{dot}} = \sum_{\sigma=\uparrow,\downarrow} \varepsilon_d d^\dagger_\sigma d_\sigma + U d^\dagger_\uparrow d_\uparrow d^\dagger_\downarrow d_\downarrow, \tag{1.2}$$

where $d^\dagger_\sigma$ and d_σ are second-quantized creation and annihilation operators. The first term is an on-site energy and the second term penalizes double occupation with the Coulomb repulsion. Since the quantum dot is embedded in a 2D electron gas we have to also include a term that accounts for that. Within Fermi liquid theory [26], the interactions of the electron gas simply renormalize the electron mass and we can write the Hamiltonian of the electron gas in a non-interacting form

$$H^{\text{bath}} = \sum_{\vec{k},\sigma} \varepsilon_{\vec{k}} c^\dagger_{\sigma\vec{k}} c_{\sigma\vec{k}}, \tag{1.3}$$

where $\vec{k}$ are the quasi momenta of the emergent quasi-particles. The total Hamiltonian of a quantum dot embedded in an electron gas is therefore given by

$$H = H^{\text{dot}} + H^{\text{mix}} + H^{\text{bath}}, \tag{1.4}$$

with a mixing Hamiltonian given by

$$H^{\text{mix}} = \sum_{\vec{k},\sigma} \left[V_{\vec{k}} d^\dagger_\sigma c_{\vec{k}\sigma} + h.c. \right], \tag{1.5}$$

where $V_{\vec{k}}$ gives the strength of the tunnel-coupling between the bath and the dot. We can imagine that with an appropriate tuning of ε_d and U we can end up in a situation where the dot is simply occupied by a single electron. The spin orientation of the electron measured along an arbitrary direction can either be up or down, though before measurement the spin is in a superpositions of both orientations which is precisely the desired behaviour of a qubit. This claim will be investigated numerically in detail in chapter 3.

Eq. (1.4) is known in the Condensed Matter community as the Anderson Impurity model [27]. At this stage the dot is coupling via $V_{\vec{k}}$ to all the momenta $\vec{k}$, though in the next chapter we will transform the Hamiltonian to a simple nearest-neighbor interaction chain Hamiltonian, this is visualized in Fig. 1.3.

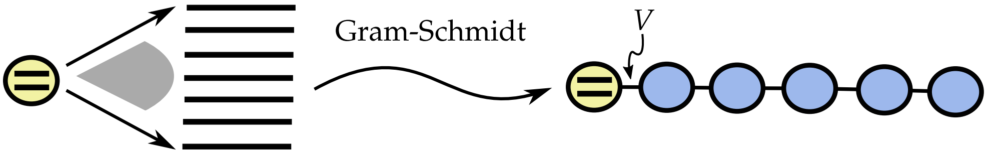

Figure 1.3: The dot (in yellow) couples to all momenta $\vec{k}$ (indicated by the black horizontal lines), a Gram-Schmidt procedure allows to rewrite the Hamiltonian in a new basis (Wilson basis), where it is a simple nearest-neighbor interaction chain Hamiltonian. The blue dots indicate the conduction sites of the chain Hamiltonian in the new basis, this will be discussed in detail in section 2.1.

1.1.3 Quantum Dot coupled to an Electronic Cavity

The next step towards building a quantum computer is finding means of efficiently entangling spatially separated quantum dots, since a single qubit on its own is not very useful. To perform meaningful calculations we need a macroscopic number of quantum dots that are entangled, thus fully utilizing the quantumness that allows for calculations that are classically not possible. One proposed possibility is to use an electronic cavity [11]. An electronic cavity is a geometrical confinement that generates standing electron waves. The eigen modes of the cavity have associated eigen-energies that can be populated by electrons. Since the electrons in the electronic cavity are not spatially confined, as in the dot, the Coulomb interaction can be neglected. For our discussion we will assume that the electronic cavity has a single doubly-degenerate energy level. The experimental realization of this is reported in Ref. [11, 12]. Fig. 1.4 shows a sketch of the experimental setup. The electronic cavity, in green, is generated by the parabola shaped electrode, in black, focusing on the quantum dot, in yellow. The dot is controlled by the electrodes surrounding it, the arrows indicate localized dot and electronic cavity electrons. The properties of the experimental setup are analysed by applying a voltage between the left and right side. The electrons have to tunnel through the quantum dot and cavity and thus give information about its physical properties. The experiment has already undergone theoretical investigation in Ref. [13] where a model Hamiltonian

$$H = H^{\text{dot}} + H^{\text{cav}} + H^{\text{bath}} + H^{\text{mix}} + H^{\text{dot-cav}}, \tag{1.6}$$

was proposed that comprises the system into a left and a right part. The bath consists of a left and right conduction part which couples to the dot via t_L and the electronic cavity via t_R which are again coupled via Ω. The baths can be set to different chemical potentials and thus allows to analyse the properties of the current that were observed in the experiments in Ref. [11, 12].

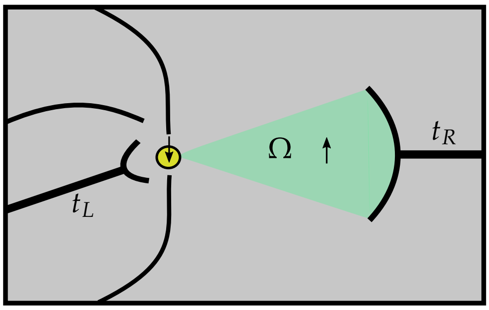

Figure 1.4: Sketch of the experimental dot-cavity setup. A detailed description of the specific experimental parameters can be found in Ref.[12].

The Hamiltonian of the electronic cavity is given by

$$H^{\text{cav}} = \sum_{\sigma} \varepsilon_\sigma c^\dagger_\sigma c_\sigma \,, \tag{1.7}$$

where $c^{(\dagger)}_\sigma$ are the fermionic operators of the electronic cavity, we will limit our discussion to a single cavity energy level, though it can trivially be extended to include an arbitrary amount. The mixing is given by

$$H^{\text{mix}} = \sum_{\vec{k},\sigma} \left[t_L \left[d^\dagger_\sigma c_{\vec{k}\sigma L} + h.c. \right] + t_R \left[c_\sigma c^\dagger_{\vec{k}\sigma R} + h.c. \right] \right] \tag{1.8}$$

and the dot-cavity coupling is defined as

$$H^{\text{dot-cav}} = \sum_{\sigma} \Omega \left[d_\sigma c^\dagger_\sigma + h.c. \right] . \tag{1.9}$$

Just like for the dot, we can visualize the structure of the Hamiltonian, see Fig. 1.5, which should make clear how the couplings in the model Hamiltonian are connected to the experiment seen in Fig. 1.4.

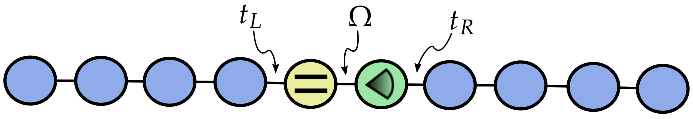

Figure 1.5: Visualization of the dot-cavity Hamiltonian in the Wilson basis (as described in Fig. 1.3). The dot in yellow and electronic cavity in green couple to the left and right conduction sites in blue via t_L and t_R. Dot and cavity are coupled by Ω.

1.1.4 The Anderson Impurity Model

The Anderson Impurity model, introduced in Eq. (1.4), has a rich theoretical history in Condensed Matter Theory. It was first formulated in the 1960s by Anderson to describe localized magnetic states in metals [27]. Anderson used the Hamiltonian in Eq. (1.4) to derive the necessary conditions for the formation of localized magnetic moments on iron-group ions dissolved in nonmagnetic metals. The picture for Anderson's original Hamiltonian is that H_{dot} describes the d-shell of the impurity with U being the Coulomb integral of the spin up and down electrons

$$U = \int |\varphi_d(\mathbf{r}_1)|^2 |\varphi_d(\mathbf{r}_2)|^2 e^2 |\mathbf{r}_1 - \mathbf{r}_2| d\tau_1 d\tau_2. \tag{1.10}$$

The electrons of the localized d orbital mix with the conduction electrons via H^{mix}, where the strength of the coupling is given by $V_{\vec{k}}$ which is the matrix element for going from the d-level to a state of momentum $\vec{k}$ above the Fermi surface. We will numerically investigate these phenomena in the following chapter.

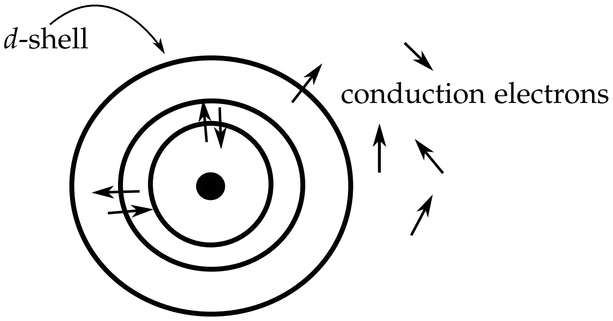

Figure 1.6: Impurity ion with a single occupied d-level, embedded in a Fermi sea of conduction electrons. The circles denote the orbitals of the impurity ion and the arrows symbolize the electron spin.

For $V_{\vec{k}} \to 0$, $\varepsilon_d < 0$ and $\varepsilon_d + U$ the ground state is given by the filled Fermi sea and a single electron occupying the d orbital. For small but finite $V_{\vec{k}}$, i.e. $r_\uparrow = \Gamma/|\varepsilon_d| \ll 1$ and $r_\downarrow = \Gamma/|\varepsilon_d + U| \ll 1$ the situation becomes more interesting and the spin states are mixed by electrons hopping on and off the d orbital with an interaction rate Γ, given by

$$\Gamma = \pi |V_{\vec{k}}|^2 \rho(\varepsilon), \tag{1.11}$$

where $\rho(\varepsilon)$ is the density of the conduction band states (this directly follows from Fermi's golden rule)[21]. An interesting question is how the conduction states can screen the localized impurity momentum and in which parameter regime of U and $V_{\vec{k}}$ the transition between non-screened and screened momenta is happening. The answer to this question turns out to be a difficult many-body problem and cannot be treated in a one-electron approximation. The difficulty arises due to spin scattering. Let us imagine two electrons of the conduction band scattering with the spin of the localized state, as shown in Fig. 1.7. Two successive electrons cannot undergo independent spin-flip scatterings by the same localized electron because the first conduction electron changes the spin of the localized state. This means that the scattering process of the second electron depends on the previous electron and the problem therefore has to be treated as a many-body problem and not in a one-electron approximation, see Ref. [28, 29] for a more detailed discussion.

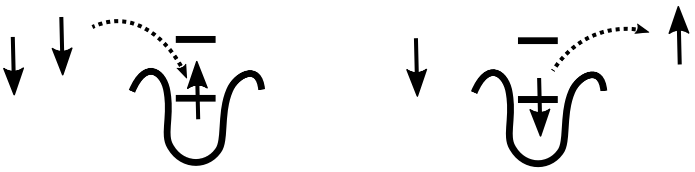

Figure 1.7: Successive scattering of two conduction band electrons with the dot spin. The first scattering flips the spin, the second electron cannot undergo spin-flip scattering. The first electron thus influences the scattering of the second electron.

All of the above directly applies to the quantum dot and we thus see that the quantum dot is an experimental realization of the Anderson Impurity model that allows to probe the wide variety of quantum many-body phenomena that are described by the model. We will thus use the terms Anderson Impurity, quantum dot and artificial atom interchangeably.

1.1.5 The Kondo Problem

A seemingly unrelated problem plagued theoretical physicists in the 1960s, known as the Kondo problem. It denotes the inability to describe the resistance minimum occurring in metals at low, but finite temperatures, when containing a small concentration of magnetic impurities, as shown in Fig. 1.8. It was expected that the inelastic scattering is reduced with decreasing temperature and the resistivity should therefore monotonically decrease with the temperature T. From the first observation of the effect in 1934 [15], it took three decades until Kondo [6] proposed his Hamiltonian, that provided a simple physical picture and explained the experimental data. The Kondo model

$$H = H^{\mathrm{K}} + H^{\mathrm{bath}}, \tag{1.12}$$

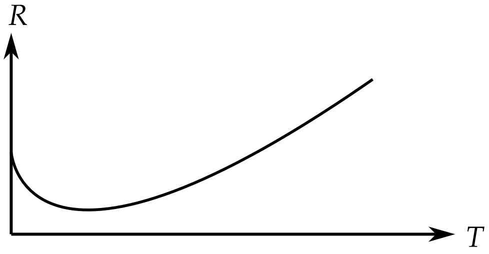

Figure 1.8: Schematic plot of the resistivity R of a metal with a small concentration of magnetic impurities as a function of temperature T. The increase in resistivity for low temperature T is caused by Kondo scattering.

consists of a simple non-interacting electron gas, as seen in Eq. (1.3) and a localized magnetic moment $\vec{S}$ of the impurity

$$H^{\mathrm{K}} = J\vec{S} \cdot \vec{s}_{\mathrm{bath}}, \tag{1.13}$$

interacting with the spin of the conduction electrons

$$\vec{s}_{\mathrm{bath}} = \frac{1}{2N} \sum_{\vec{k}\vec{k}'} \sum_{\alpha\beta} c^{\dagger}_{\vec{k}\alpha} \vec{\sigma}_{\alpha\beta} c_{\vec{k}'\beta}, \tag{1.14}$$

where $\vec{\sigma}$ are the Pauli matrices and N is the number of conduction electrons, the value of the coupling J is not fixed by the theory. Even though phonons freeze out for $T \to 0$, spin flip scattering is still possible and provides a residual scattering mechanism for conduction electrons. Kondo was able to calculate the resistivity perturbatively,

$$R \propto J^2 - J^3 \rho(\varepsilon_F) log(\frac{k_B T}{D}), \tag{1.15}$$

where $\rho(\varepsilon_F)$ is the density of states at the Fermi surface ε_F and D the width of the density of states. This describes the resistivity minima, but diverges for $T \to 0$. The perturbative result breaks down in this regime, because the scattering rate becomes of the order $\mathcal{O}(1)$ at temperatures of an exponentially small energy scale

$$T_{\mathrm{K}} \propto De^{-\frac{1}{\rho J}}, \tag{1.16}$$

known as the Kondo temperature. We have already encountered this spin flip scattering which is causing the break down of perturbation theory in the Anderson Impurity model. This similarity is the first indication of the deep connection between the Anderson Impurity model and the Kondo model.

In fact, the are approximately related by a simple unitary transformation, as detailed below.

1.1.6 Schrieffer Wolff transformation

Starting form the Anderson Impurity model, Eq. (1.4), Schrieffer and Wolff [21] noted that the break down of perturbation theory for small but finite $V_{\vec{k}}$ is caused by arbitrary small energy denominators entering in the perturbative expansion, due to the spin flip scattering. One can isolate the interactions which dominate the dynamics for small $V_{\vec{k}}$ by performing a unitary transformation which eliminates $V_{\vec{k}}$ to first order

$$H' = e^S H e^{-S} \tag{1.17}$$

which is required to have no terms of first order in $V_{\vec{k}}$. Denoting the terms in Eq. (1.4) not involving $V_{\vec{k}}$ as H_0 and the term involving $V_{\vec{k}}$ as H_1 one has

$$H' = H_0 + \frac{1}{2}[S, H_1] + \frac{1}{3}[S, [S, H_1]] + \frac{1}{8}[S, [S, [S, H_1]]] + \cdots, \tag{1.18}$$

where the first order $V_{\vec{k}}$ are eliminated with the condition

$$[H_0, S] = H_1 \tag{1.19}$$

which determines the generator S. Schrieffer and Wolff showed that H' is well approximated by the first two terms for small $V_{\vec{k}}$ which is simply the Kondo interaction term, Eq. (1.13), with an effective coupling

$$J^{\text{eff}} = 2|V_{\vec{k}}|^2 \frac{U}{\varepsilon_d(\varepsilon_d + U)} < 0. \tag{1.20}$$

We thus conclude that the Anderson Impurity model can be replaced by the Kondo model for $r_\alpha \ll 1$, i.e. $T < T_{\text{K}}$. Plugging the effecive coupling J^{eff} into Eq. (1.16) yields

$$T_{\text{K}} \propto D \exp\left(-\frac{\varepsilon_d(\varepsilon_d + U)}{2|V_{\vec{k}}|^2 U \rho} \right) \tag{1.21}$$

for the Kondo temperature T_{K} below which perturbation theory breaks down.

1.1.7 Kondo Resonance and Kondo Singlet

The ground state of the Kondo model for $T < T_K$ cannot be accessed perturbatively because conduction electrons continuously scatter with the impurity spin which causes the spin to flip from up to down and the other way around. This many-body process places the impurity in a singlet ground state with the spin polarization of the conduction electrons, known as Kondo singlet, see Ref. [29, 21]. The conduction electrons that scatter with the impurity are energetically closely positioned around the Fermi energy and cause a resonance peak in the density of states.

Chapter 2

Methods

In this chapter we present the numerical methods that we used over the course of our work. In particular, it comprises the Numerical Renormalization Group that allows to rewrite the Hamiltonian of our models in a numerically tameable form, the Matrix Product State representation and the Density Matrix Renormalization Group that will be our main computational tools as well as the Quantum Information Approach. A discussion of the Kernel Polynomial Method is presented in Appendix D.

2.1 Numerical Renormalization Group

It was not until the 1970s that Wilson [22] developed a fully non-perturbative technique that allowed for a complete solution of the Kondo and Anderson Impurity model. Wilson developed the idea of Renormalization Group (RG) into a numerical scheme that gave great insight into the underlying physics of the Kondo problem which is known today as the Numerical Renormalization Group (NRG), a review on the matter can be found in Ref. [17]. Wilson's NRG can be applied to all quantum impurity problems, where the term quantum impurity denotes a system with the following structure: a quantum mechanical system with a small number of interacting degrees of freedom, the impurity, coupled to a non-interacting bath of fermions or bosons, usually with a continuous excitation spectrum, just like the dot-cavity setup. There is no restriction on the structure of the impurity except for its small number of degrees of freedom that allows it to be diagonalized exactly. In the following discussion we will focus on fermions, though the discussion can equally be carried out for bosons. The model can thus be written as

$$H = H^{\mathrm{imp}} + H^{\mathrm{bath}} + H^{\mathrm{mix}}, \tag{2.1}$$

where H^{imp} describes the impurity, H^{bath} the non-interacting bath of fermions in the conduction band and H^{mix} the mixing between the impurity and the bath. The bath and mixing Hamiltonians are given by

$$\begin{aligned} H^{\text{bath}} &= \sum_{\vec{k}\sigma} \varepsilon_{\vec{k}} c^{\dagger}_{\vec{k}\sigma} c_{\vec{k}\sigma} \\ H^{\text{mix}} &= \sum_{\vec{k}\sigma} \left[V_{\vec{k}} d^{\dagger}_{\sigma} c_{\vec{k}\sigma} + h.c. \right], \end{aligned} \tag{2.2}$$

where $c^{(\dagger)}_{\vec{k}\sigma}$ are the fermionic operators of the conduction band states with spin σ and energy $\varepsilon_{\vec{k}}$ and $d^{(\dagger)}_{\sigma}$ are the operators corresponding to the impurity with energy ε_d, just like in the Anderson Impurity model 1.6. The energies $\varepsilon_{\vec{k}}$ and ε_d are measured from the Fermi level. The coupling between the impurity and bath is described by the bath coupling $V_{\vec{k}}$. The conduction band is assumed to be symmetric and lies within the interval $\left[-D, D \right]$, we will set $D = 1$ for all further discussions. For our further analysis it is convenient to rewrite the Hamiltonian in its energy representation rather than the momentum representation. The reformulation is not unique, one such reformulation is given by

$$H = H^{\text{imp}} + \sum_{\sigma} \int_{-1}^{1} \mathrm{d}\varepsilon \, \rho(\varepsilon) a^{\dagger}_{\varepsilon\sigma} a_{\varepsilon\sigma} + \sum_{\sigma} \int_{-1}^{1} \mathrm{d}\varepsilon \, h(\varepsilon) \left[d^{\dagger}_{\sigma} a_{\varepsilon\sigma} + a^{\dagger}_{\varepsilon\sigma} d_{\sigma} \right], \tag{2.3}$$

where $\rho(\varepsilon)$ is the density of states and $h(\varepsilon)$ describes the interaction between the impurity and the bath. The equivalence of Eq. (2.2) and Eq. (2.3) can be shown by integrating over the conduction electron degrees of freedom which leads to the same effective impurity action as the momentum formulation, see Ref. [30] for a detailed discussion. The operators $a^{(\dagger)}_{\varepsilon\sigma}$ create or annihilate an electron in an s-wave state of energy ε.

2.1.1 Logarithmic discretization

The goal of our calculation is to obtain the impurity contribution to the various properties of the system. At the heart of the NRG calculations for quantum impurity problems lies a logarithmic discretization that allows to discretize a continuous, non-interacting conduction band,

$$H^{\text{bath}} = \sum_{\sigma} \int_{-1}^{1} \mathrm{d}\varepsilon \, \rho(\varepsilon) a^{\dagger}_{\varepsilon\sigma} a_{\varepsilon\sigma} \tag{2.4}$$

in a way that retains information about the underlying physics at energy scales $\Lambda^{-n/2}$, where Λ is a discretization parameter, thus giving high resolution around the Fermi energy. The discretization will yield a hopping

Hamiltonian

$$H^{\text{bath}} = \sum_{\sigma n=0}^{\infty} \left[\varepsilon_n c^\dagger_{n\sigma} c_{n\sigma} + t_n \left[c^\dagger_{n\sigma} c_{n+1\sigma} + c^\dagger_{n+1\sigma} c_{n\sigma} \right] \right], \tag{2.5}$$

with exponentially decaying hoppings, $t_n \propto \Lambda^{-n/2}$.

The first step to achieve this, is to discretize the continuum of energies ε in the interval $-1 \leq \varepsilon \leq 1$. We choose discrete points $\varepsilon_n = \pm \frac{1}{\Lambda^n}$ which yields log-spaced points in the conduction band, as shown in Fig. 2.1. In every interval between a pair of points $[\pm\frac{1}{\Lambda^{n-1}}, \pm\frac{1}{\Lambda^n}]$, we rewrite the operators in terms of their Fourier decomposition

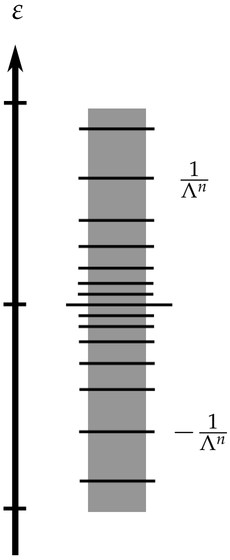

Figure 2.1: Logarithmic discretization of the conduction band. Horizontal lines indicate the points in energy space where the fermionic operators are expanded in its Fourier decomposition. This figure was adapted from Ref. [22].

$$a_{\varepsilon\sigma} = \sum_{np} \left[a_{np\sigma} \psi^+_{np}(\varepsilon) + b_{np\sigma} \psi^-_{np}(\varepsilon) \right] \tag{2.6}$$

where

$$\psi^{\pm}_{np}(k) = \begin{cases} \frac{1}{\sqrt{\Delta_n}} e^{\pm i \omega_n p \varepsilon} & \text{if} \frac{1}{\Lambda^{n-1}} < \varepsilon < \frac{1}{\Lambda^n}, \\ 0 & \text{if } \varepsilon \text{ is outside the above interval.} \end{cases} \tag{2.7}$$

$\Delta_n = \frac{1}{\Lambda^{n-1}} - \frac{1}{\Lambda^n}$ is the interval width and $\omega_n = 2\pi/\Delta_n$ the corresponding Fourier frequency. Here n, the interval index, takes values $0, 1, 2, ...$ and p, the Fourier index, takes all integer values from $-\infty$ to $+\infty$, the superscript $\pm$ denotes basis functions defined for positive and negative energy. The wave functions $\psi^{\pm}_{np}(k)$ vanish outside their corresponding interval, thus the sum over n only has contributions for the corresponding n^{th} energy window.

The operators $a^{(\dagger)}$ and $b^{(\dagger)}$ fulfill the usual fermionic commutation relations

$$\{a_{np\sigma}, a^{\dagger}_{n'p'\sigma'}\} = \delta_{nn'}\delta_{pp'}\delta_{\sigma\sigma'} \tag{2.8}$$

$$\{b_{np\sigma}, b^{\dagger}_{n'p'\sigma'}\} = \delta_{nn'}\delta_{pp'}\delta_{\sigma\sigma'}, \tag{2.9}$$

where $a^{(\dagger)}$ anti-commutes with $b^{(\dagger)}$.

We now insert Eq. (2.6) into H^{bath} and H^{mix} and neglect all terms with $p \neq 0$. Plugging the discretized operators, Eq. (2.6), into the original Hamiltonian in the energy basis, Eq. (2.3). It can be shown that the impurity only couples to the $p = 0$ components of the conduction band and the coupling between the $p = 0$ and $p \neq 0$ has a prefactor $1 - \Lambda^{-1}$ that vanishes in the continuum limit $\Lambda \to 1$. It turns out that the results obtained for values of Λ as large as $\Lambda = 2$ give surprisingly good results and we will thus use $\Lambda = 2$ for all our numerical calculations. It is therefore numerically justified to drop the $p \neq 0$ terms. See Ref. [17, 22] for details.

Finally, after some algebra, we obtain the discretized Hamiltonian

$$\begin{aligned} H = H^{\text{imp}} &+ \sum_{n\sigma} \left[\xi^{+}_{n} a^{\dagger}_{n\sigma} a_{n\sigma} + \xi^{-}_{n} b^{\dagger}_{n\sigma} b_{n\sigma}\right] \\ &+ \frac{1}{\sqrt{\pi}} \sum_{n\sigma} d^{\dagger}_{\sigma} \left[\gamma^{+}_{n} a_{n\sigma} + \gamma^{-}_{n} b_{n\sigma}\right] \\ &+ \frac{1}{\sqrt{\pi}} \sum_{n\sigma} \left[\gamma^{+}_{n} a^{\dagger}_{n\sigma} + \gamma^{-}_{n} b^{\dagger}_{n\sigma}\right] d_{\sigma}, \end{aligned} \tag{2.10}$$

the coupling amplitudes $\xi^{\pm}_{n}$ and $\gamma^{\pm}_{n}$ are given by

$$\gamma^{\pm^2}_{n} = \int^{\pm,n} d\varepsilon\, \Gamma(\varepsilon), \tag{2.11}$$

$$\xi^{\pm}_{n} = \frac{\int^{\pm,n} d\varepsilon\, \Gamma(\varepsilon)\varepsilon}{\gamma^{\pm^2}_{n}}, \tag{2.12}$$

where $\int^{+,n} d\varepsilon \equiv \int_{\varepsilon_{n+1}}^{\varepsilon_n} d\varepsilon$ and $\int^{-,n} d\varepsilon \equiv \int_{-\varepsilon_n}^{-\varepsilon_{n+1}} d\varepsilon$ and $\Gamma(\varepsilon)$ defined in Eq. 1.11.

At this step we have not gained much since the impurity operators $d^{(\dagger)}_{n}$ couple to all operators $a^{(\dagger)}_{n\sigma}$ and $b^{(\dagger)}_{n\sigma}$ of the conduction band and it is still a hopeless encounter to diagonalize the Hamiltonian for any macroscopic number of states.

2.1.2 Conversion to a hopping Hamiltonian

As a next step we aim at transforming the Hamiltonian into a simpler form, say a nearest neighbor hopping form, as seen in Eq. (2.5). Thus we need to transform the operators $a_{n\sigma}^{(\dagger)}$ and $b_{n\sigma}^{(\dagger)}$ into a new orthogonal basis $c_{n\sigma}$. Starting with $c_{0\sigma}$, we define

$$c_{0\sigma} = \frac{1}{\sqrt{\xi_0}} \sum_n \left[\gamma_n^+ a_{n\sigma} + \gamma_n^- b_{n\sigma}\right]. \tag{2.13}$$

Considering the general structure of an orthogonal transformation, one can write

$$c_{n\sigma} = \sum_m \left[u_{nm} a_{m\sigma} + v_{nm} b_{m\sigma}\right], \tag{2.14}$$

with the usual requirements

$$u^T u = u u^T = \mathbb{1} \tag{2.15}$$

for the matrices u and v. The inverse is given by

$$a_{n\sigma} = \sum_m u_{mn} c_{m\sigma} \quad \text{and} \quad b_{n\sigma} = \sum_m v_{mn} c_{m\sigma}. \tag{2.16}$$

Comparing Eq. (2.13) and Eq. (2.14) we can read off the coefficients

$$u_{0m} = \frac{1}{\sqrt{\xi_0}} \gamma_m^+ \quad \text{and} \quad v_{0m} = \frac{1}{\sqrt{\xi_0}} \gamma_m^-, \tag{2.17}$$

thus fixing c_0. The same considerations can be carried out for all other $c_{n\sigma}$ which yields recursion relations for t_n and ε_n that can be found in Ref. [17] and have to be implemented numerically. For the case of a constant density of states of the conduction electrons the hoppings can be calculated analytically,

$$t_n = \frac{(1+\Lambda^{-1})(1-\Lambda^{-n-1})}{2\sqrt{(1-\Lambda^{-2n-1})}\sqrt{(1-\Lambda^{-2n-3})}} \Lambda^{-n/2} \tag{2.18}$$

which simplifies to $t_n \propto \Lambda^{-n/2}$ for large n. The on-site energies ε_n are simply zero. The details of Wilson's ingenuous unitary transformation can be found in Ref. [22]. We will call this new basis Wilson basis.

2.1.3 Numerical Renormalization Group in its classical formulation

Using the logarithmic discretization that was described in section 2.1.1, we are able to rewrite the quantum impurity Hamiltonian in the Wilson basis where the impurity only directly couples to the zero$^{\text{th}}$ Wilson state, as seen in Fig. 2.2.

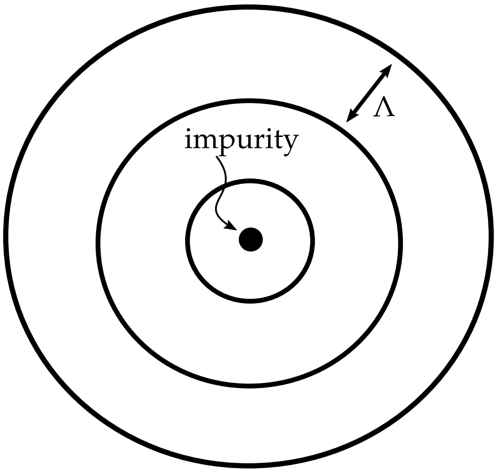

Figure 2.2: Onion-like spherical shells, where each shell represents a state in the Wilson basis. The impurity lies at the Fermi energy and is surrounded by Wilson states, each ring represents a state that is created by $c^\dagger_{n\sigma}$ with energies of order $\Lambda^{-n/2}$. With increasing radii we are moving away from the Fermi energy. This figure was adapted from Ref. [22].

The final quantum impurity Hamiltonian is given by

$$H = H^{\text{imp}} + V \sum_{\sigma} \left[d^\dagger_\sigma c_{0\sigma} + c^\dagger_{0\sigma} d_\sigma \right] + \sum_{\sigma n=0}^{\infty} \left[\varepsilon_n c^\dagger_{n\sigma} c_{n\sigma} + t_n \left[c^\dagger_{n\sigma} c_{n+1\sigma} + c^\dagger_{n+1\sigma} c_{n\sigma} \right] \right], \tag{2.19}$$

where we assumed a $\vec{k}$ independent bath coupling $V_{\vec{k}} = V$. The reason we went through the trouble of Wilson's transformation will become clear once we take a closer look at the couplings t_n. Due to the log-spacing of the discretization they turn out to be exponentially decaying.

If we look at the bath term of the logarithmically discretized quantum impurity Hamiltonian

$$H^{\text{bath}} = \sum_{\sigma} t_0 \left[c^\dagger_{0\sigma} c_{1\sigma} + h.c \right] + t_1 \left[c^\dagger_{1\sigma} c_{2\sigma} + h.c \right] + t_2 \left[c^\dagger_{2\sigma} c_{3\sigma} + h.c \right] + ..., \tag{2.20}$$

each hopping term is probing a different energy scale given by $\Lambda^{-n/2}$ as seen in Fig. 2.3.

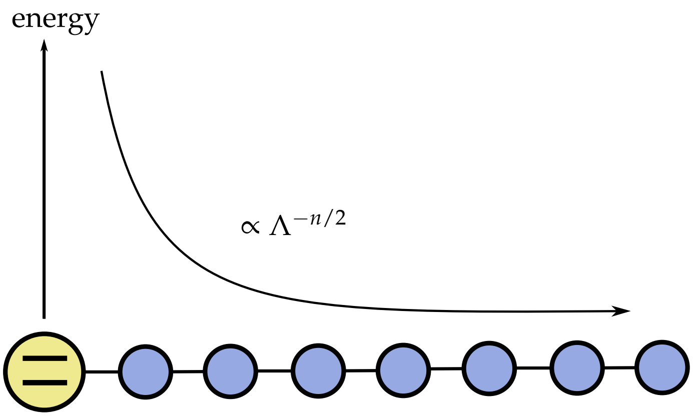

Figure 2.3: Schematic visualization of the quantum impurity chain Hamiltonian. The energy scale decreases as $\Lambda^{-n/2}$ as we are walking along the chain. The first site symbolizes the impurity, further sites are the conduction band sites.

It is this structure of the problem, that motivates us to use a Renormalization Group approach. We start off by fully diagonalizing the isolated impurity H^{imp}, this yields exact eigenstates and eigen-energies for the impurity. As a next step, we add the first conduction electron site of H^{bath} and diagonalize the Hamiltonian matrix of the enlarged Hilbert space. This procedure is then iterated. The obvious problem of this approach is that the Hilbert space grows as d^N, where d is the local Hilbertspace dimension, say 4 in the occupation basis $\{|0\rangle, |\uparrow\rangle, |\downarrow\rangle, |\uparrow\downarrow\rangle\}$, and N is the conduction site index. This makes it impossible to keep all the states in the calculation and we need to devise some truncation of the states that allows to keep the matrix dimension constant during the iteration. Due to the exponentially decaying hoppings, we are going down in energy during the iteration, this means that the resolution of high energy states gets worse as we are iteratively diagonalizing the Hamiltonian. Wilson [22] thus devised a very simple truncation procedure in which only the states with the lowest eigen-energies are kept. Thus for every iteration we obtain a number of eigenstates and energies at energy scale $\Lambda^{-n/2}$. This is a quasi excitation spectrum of the full Hamiltonian which can be used to obtain the partition function

$$Z = \sum_n e^{-E_n/k_B T}, \tag{2.21}$$

from which all thermodynamic physical properties can be derived, see Ref. [17, 31] for a detailed discussion.

The flow of these energies as a function of the site index is called RG flow and provides additional information about the underlying physics. If the energies remain unchanged along the chain this is called a fixed point which means that the described physics is independent of the energy scale. Once the energies move, this means that we are probing different physics and thus a different effective Hamiltonian. This can give us informations about the different physics described by a given Hamiltonian and at which energy scale they dominate. In the Anderson Impurity model for example one observes three distinct fixed points, starting with the free-orbital fixed point which is an Anderson Impurity model with $U = 0$ and $V = 0$, it crosses over to the local-momentum fixed point, which is a free spin decoupled from the conduction electrons and finally crosses over to the stable strong-coupling fixed point $V \to \infty$ where the spin is screened [17]. The fixed point Hamiltonians are found by comparing the spectrum of the NRG with the spectrum of the proposed Hamiltonian.

2.2 Matrix Product States

Rather than following the NRG procedure, developed by Wilson [22] and presented in the previous section, we will choose a more modern approach to tame the exponential scaling of the Hilbert space. This approach is known as the Matrix Product State (MPS) approach and is based on a polynomially scaling representation of states.

To motivate this representation, let us take a look at the basic work flow of quantum mechanics:

- choose a basis $\{|\Phi_1\rangle, |\Phi_2\rangle, ..., |\Phi_n\rangle\}$,
- write down the Hamiltonian in terms of that basis, $H_{nm} = \langle\Phi_n| \hat{H} |\Phi_m\rangle$
- and solve the Schrödinger equation, $H_{nm} |\psi_m\rangle = E_n |\psi_m\rangle$, by diagonalizing the Hamiltonian.

Let us test this approach on a very simple problem, a 1D chain of L spin $\frac{1}{2}$ fermions. As a computational basis we choose the projection of the spin in the z direction, thus for each fermion we have a local (on one specific site) $\{|\uparrow\rangle, |\downarrow\rangle\}$ basis. An arbitrary state can thus be expressed as

$$|\psi\rangle = \sum_{\sigma_1,...,\sigma_L} c_{\sigma_1...\sigma_L} |\sigma_1\rangle \otimes |\sigma_2\rangle \otimes ... \otimes |\sigma_L\rangle \tag{2.22}$$

where $|\sigma_i\rangle$ denotes the local state, in our case either spin up or down. Physically speaking, we are writing an arbitrary state as a superposition of all the basis vectors weighted with coefficients $c_{\sigma_1...\sigma_L}$. Diagonalizing the Hamiltonian would give us the appropriate coefficients to express any eigenstate, say the ground state.

Before we embark on that endeavor we should think about the dimensionality of the Hamiltonian matrix. Since every local state $|\sigma_i\rangle$ has two possible states and the tensor product is just multiplying the dimensions our arbitrary state, $|\psi\rangle$ will be a 2^L dimensional object. Thus making the Hamiltonian matrix $2^L \times 2^L$ dimensional.

Conventional dense matrix diagnoalization algorithms scale as $O(N^3)$ where N is the dimension of the matrix. Plugging in some numbers, we find that for a spin chain of 100 spin $\frac{1}{2}$ fermions a diagonalization will scale as $O(2^{300}) \approx 10^{90}$ which is 60 orders of magnitude more than the age of the universe. Thus exactly solving any quantum mechanical problem with a macroscopic number of particles is seemingly an impossible task. However, it turns out that to describe reality we only need to explore a significantly smaller part of the full Hilbert space. Therefore, we want to find a way to restrict ourselves to a subspace in Hilbert space which gives us a set of states that approximates nature in a meaningful way.

This problem lies at the heart of computational quantum mechanics and has led to the development of ingenious algorithms ranging form density functional theory [32] to quantum monte carlo [33], tensor networks and neural networks as its latest extension [34]. For our purposes we will be using tensor networks or also known as Matrix Product States. Matrix Product States will allow us to compactly store and represent states as well giving us an intuitive way of finding the ground state.

2.2.1 Singular Value Decomposition

We have seen that exactly diagonalizing the Hamiltonian is a seemingly impossible task due to the exponential scaling of the Hilbert space dimension. To compress the Hamiltonian and wave function we will use a simple tool from linear algebra, the singular value decomposition of a rectangular matrix. Given a $m \times n$ matrix M we can decompose M as

$$M = USV^{\dagger}, \tag{2.23}$$

where

- U is an $m \times m$ unitary matrix,
- S is a diagonal $m \times n$ matrix with positive real numbers on the diagonal and
- $V^{\dagger}$ is an $n \times n$ unitary matrix.

Looking at Eq. (2.22) we can arrange the coefficients $c_{\sigma_1 \ldots \sigma_L}$ of the state vector $|\psi\rangle$ into a highly rectangular matrix $2 \times 2^{L-1}$ where the two rows contain the coefficients for the spin up and down states and decompose it via a singular value decomposition. This means that we have split the system into two parts that are connected via the singular value matrix S. The eigenvalues in S give us a measure of how much the two parts are entangled. If we only have a single eigenvalue in S it means that the two split systems are completely independent of each other and can just be decomposed without loosing any information. If we now arrange the singular values in S in descending order we can cut off beneath some threshold value, thus reducing the size of the matrix. More formally we have

$$c_{\sigma_1 \dots \sigma_L} = \sum_{a_1}^{D} U_{\sigma_1 a_1} S_{a_1 a_1} V^{\dagger}_{a_2 \sigma_3 \dots \sigma_L} \tag{2.24}$$

where D is our cut off which is called the bond dimension. Let us multiply S into $V^{\dagger}$ and continue by decomposing the resulting matrix. We can carry on with this procedure L times, resulting in

$$c_{\sigma_1 \dots \sigma_L} = \sum_{a_1 \dots a_{L-1}} A^{\sigma_1}_{a_1} A^{\sigma_2}_{a_1 a_2} \dots A^{\sigma_L}_{a_{L-1}} \tag{2.25}$$

where we have renamed the previous U matrix into A. The quantum state is now represented as a product of matrices,

$$|\psi\rangle = \sum_{\sigma_1 \dots \sigma_L} A^{\sigma_1} A^{\sigma_2} \dots A^{\sigma_L} |\sigma_1\rangle \otimes |\sigma_2\rangle \otimes \dots \otimes |\sigma_L\rangle , \tag{2.26}$$

see Ref. [16] for a thorough review on the matter.

2.2.2 Area law

The question that immediately arises, is that of the limitations of this representation. We have seen that the bond dimension D is the parameter that determines the size of the matrices and thus controls the validity of the MPS representation which is trivially exact for $D \to \infty$. The MPS representation will thus only yield a satisfactory representation of the state if the singular values in the S matrix decay rapidly, justifying a finite cut off given by the bond dimension. As already mentioned, the SVD procedure cuts the system into two parts, say A and B, given by the matrices U and $V^{\dagger}$. The singular values s_a in S are related to the entanglement entropy by

$$S_{A|B} = -\sum_a s_a^2 \log_2 s_a^2. \tag{2.27}$$

The entanglement entropy provides an entanglement measure between part A and B, see Ref. [16] for details. The area law from Quantum Information theory [35, 36] tells us that for ground states of short ranged Hamiltonians (low correlation), with a gap to the excitations, the entanglement entropy scales with the surface of the boundary region between A and B as

$$S_{A|B} \propto L^{\mathcal{D}-1}, \tag{2.28}$$

where L is the system size and $\mathcal{D}$ the spatial dimension. For $\mathcal{D} = 1$ we simply have $S_{A|B} \propto \text{const}$ which tells us that increasing the system size does not change the entanglement entropy $S_{A|B}$ which implies that the singular values in Eq. (2.27) decay such that $S_{A|B}$ stays constant and we can restrict the sum to a maximum value D, the bond dimension.

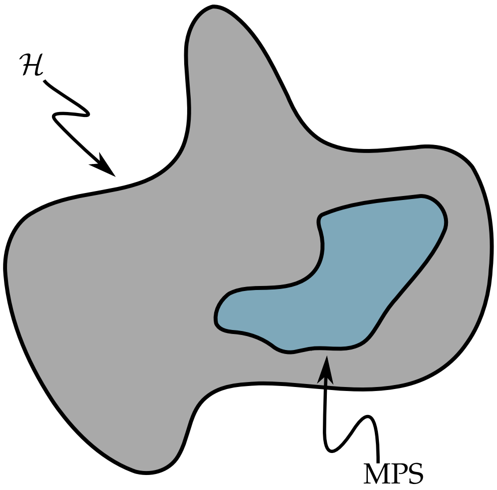

Figure 2.4: Matrix Product States span a sub space in the full Hilbert space consisting of states that represent low correlation physics.

Loosely speaking, we can picture the MPS representation as a small subregion in the vast Hilbert space that is restricted to low correlation physics, see Fig. 2.4 for a visualization.

2.2.3 Graphical representation

Until this point the MPS representation has provided us with a polynomially scaling representation of states, though in order to understand its full potential we have to first discuss a simple graphical representation of Matrix Product States. In Eq. (2.5) we have seen how the coefficients of a state in a chosen basis can be written as a product of matrices. Each matrix has three indices, σ the physical index which runs over the local Hilbert space dimensions, i.e. $0, \uparrow, \downarrow, \uparrow\downarrow$ for spinfull fermions and the matrix indices i and j that were introduced by the SVD procedure. We symbolize the matrix as a circle with three legs, one for the physical index and two for the matrix dimensions, this allows to write the MPS in a very simple way, as shown in Fig. 2.5. One can do the same SVD procedure as seen in section 2.2.1 also for

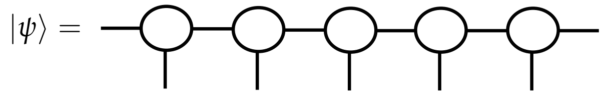

Figure 2.5: Graphical representation of a Matrix Product State. The circles symbolize the matrices in Eq. (2.5), non connected lines are the indices of the matrices and connected indices indicate contractions, i.e. a matrix product.

operators, thus yielding a Matrix Product Operator (MPO) representation of operators which gives us a very similar graphical representation [16].

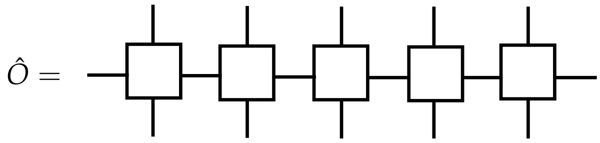

Figure 2.6: Graphical representation of a Matrix Product Operator. Boxes symbolize matrices. Non connected lines are the indices of the matrices, connected lines symbolize contractions.

To get some intuition for MPOs consider the following example. Let a Hamiltonian be build up as a tensor product of local Hamiltonians $H = H_1 \otimes H_2 \otimes H_3 \otimes \cdots \otimes H_N$, each local Hamiltonian (a matrix) is built up of some local operators, say the fermionic creation and annihilation operators which are matrices as well. This nested matrix structure is what we are representing with the multiple legs on the graphical MPO representation. Each box represents one local Hamiltonian, this allows us to construct a MPO representation of a Hamiltonian without actually writing the matrix and following the SVD procedure.

2.2.4 Quantum Impurity Matrix Product Operator

If we think about each tensor of the MPO as a transition tensor that performs a transition from one site to the next, we can graphically construct the associated tensor by collecting all the operators that make up the transition.

Let us illustrate this statement for the quantum impurity Hamiltonian Eq. (2.5), with an Anderson Impurity, Eq. (1.4), as its impurity. We first combine the coupling between the impurity V and the hoppings t into a new list $\tilde{t}_n = [V, t_0, t_1, ...]$ as well as the on-site energies $\tilde{\varepsilon} = [\varepsilon_d, \varepsilon_0^{\text{bath}}, \varepsilon_1^{\text{bath}}, ...]$ and the Hubbard term with the Coulomb interaction $\tilde{U} = [U, 0, 0, ...]$, this allows to combine the three terms H^{imp}, H^{mix} and H^{bath} into

$$H = \sum_{n\sigma} \left[[\tilde{t}_n c^\dagger_{n\sigma} c_{n+1\sigma} + h.c.] + \tilde{\varepsilon}_n c^\dagger_{n\sigma} c_{n\sigma} + \tilde{U} c^\dagger_{n\uparrow} c^\dagger_{n\uparrow} c^\dagger_{n\downarrow} c_{n\downarrow} \right]. \tag{2.29}$$

The term $H_n^{\text{on-site}} = \sum_\sigma \tilde{\varepsilon}_n c^\dagger_{n\sigma} c_{n\sigma} + \tilde{U} c^\dagger_{n\uparrow} c_{n\uparrow} c^\dagger_{n\downarrow} c_{n\downarrow}$ gives a direct transition from site n to site $n+1$, as shown in Fig. 2.7. The initial site n and final site $n+1$ can trivially transition to themselves by unity $\mathbb{1}$. The fermionic operators c and $c^\dagger$ give a transition to intermediate states, since they always appear in pairs. Fig. 2.7 shows how we can represent this statement graphically and how this translates into a tensor. We omitted the spin in the graphical construction in Fig. 2.7, though this can be trivially included by adding

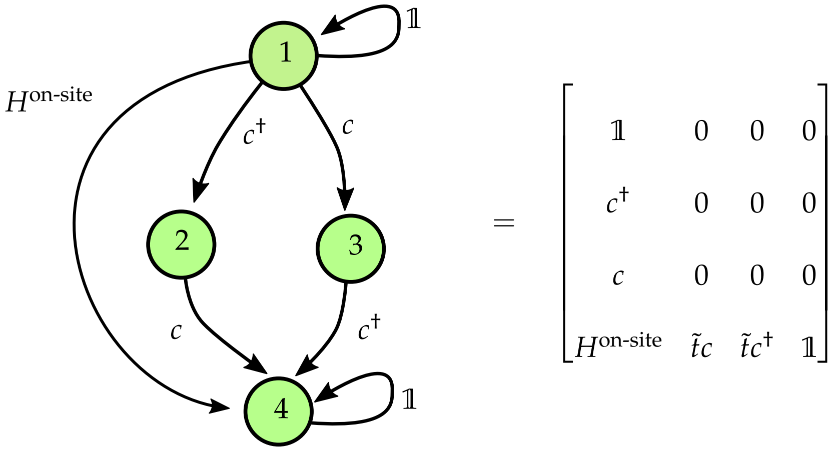
1
2
3
4
𝟙
𝟙
$H^{\text{on-site}}$
$c^\dagger$
c
c
$c^\dagger$
$=$
$\begin{bmatrix} \mathbb{1} & 0 & 0 & 0 \\ c^\dagger & 0 & 0 & 0 \\ c & 0 & 0 & 0 \\ H^{\text{on-site}} & \tilde{t}c & \tilde{t}c^\dagger & \mathbb{1} \end{bmatrix}$

Figure 2.7: Graphical MPO tensor construction. Circles represent states along the transition from site n to $n+1$, arrows indicate the transition between states with associated operators.

additional intermediate states, thus yielding the final MPO tensor

$$\begin{bmatrix} \mathbb{1} & 0 & 0 & 0 & 0 & 0 \\ c^\dagger_\uparrow & 0 & 0 & 0 & 0 & 0 \\ c^\dagger_\downarrow & 0 & 0 & 0 & 0 & 0 \\ c_\uparrow & 0 & 0 & 0 & 0 & 0 \\ c_\downarrow & 0 & 0 & 0 & 0 & 0 \\ H^{\text{on-site}} & \tilde{t}c_\uparrow & \tilde{t}c_\downarrow & \tilde{t}c^\dagger_\uparrow & \tilde{t}c^\dagger_\downarrow & \mathbb{1} \end{bmatrix} . \tag{2.30}$$

This procedure can be used to create a variety of MPOs and was used extensively throughout our work, a detailed discussion of the graphical MPO tensor construction is given in Ref. [37]. The definition of the fermionic operators can be found in Appendix A.

2.3 Density Matrix Renormalization Group

Having introduced MPS and MPOs we can now go ahead and develop a simple ground state search algorithm, know as the Density Matrix Renormalization Group (DMRG) which was invented by Steven White [38] in the early 1990s.

To find the ground state, we are looking for a state $|\psi\rangle$ that minimizes the energy expectation value $\langle\psi|\,\hat{H}\,|\psi\rangle$. This can be written as an optimization problem with a Lagrangian

$$\mathcal{L} = \langle\psi|\,\hat{H}\,|\psi\rangle - \lambda\,\langle\psi|\psi\rangle\,, \tag{2.31}$$

where the usual state normalization condition is imposed with a Lagrange multiplier λ. This translates graphically into Fig. 2.8.

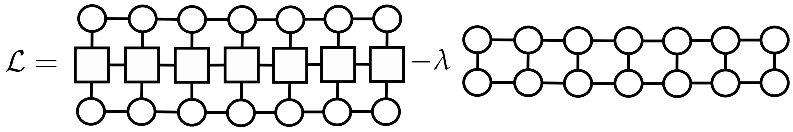

Figure 2.8: Lagrangian to be minimized for the ground state search, in graphical notation. Boxes represent the Hamiltonian in MPO form and circles represent the state in MPS form.

To find a minima we thus compute $\frac{\partial\mathcal{L}}{\partial|\psi\rangle} = 0$, unfortunately this is a highly non-linear problem because the matrices in the MPS state representation appear as products. But we can also do the optimization iteratively, instead of taking the derivative with respect to the whole MPS state, we just derive with respect to one matrix in the MPS, while keeping everything else constant.

Taking the partial derivative gets rid of one matrix in the Lagrangian, as seen in Fig. 2.9 and indicated by the hole.

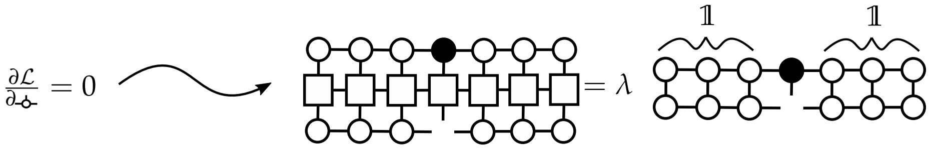

Figure 2.9: Taking the derivative with respect to one matrix in the Lagrangian Eq. (2.31) gets rid of one of the matrices, denoted by the hole, and leaves an eigenvalue problem for the black matrix.

The normalization condition, on the right side, can be contracted to unity 𝟙 by noting that the matrices U and $V^\dagger$ that were introduced in the SVD are unitary. This holds true if we keep the U matrices to the left of the current matrix and the $V^\dagger$ matrices to the right, see Ref. 2.10 for details. Generally, the collection of tensor to the left and right of the current site are called left and right environment respectively.

After taking the derivative and contracting the right part of the expression, we obtain a tensorial eigenvalue problem which looks just like the Schrödinger equation, as seen in Fig. 2.10. We will call the Hamiltonian the local Hamiltonian tensor and the eigenvector eigentensor.

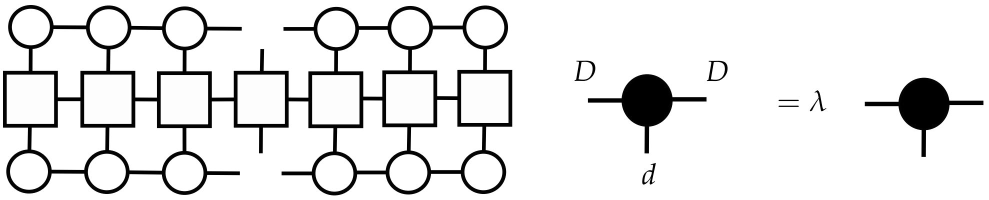

Figure 2.10: Local tensorial eigenvalue problem with a dD^2 dimensional eigentensor in black.

The local Hamiltonian tensor is reshaped into a $dD^2 \times dD^2$ matrix and diagonalized with a common diagonalization algorithm such as Lanczos. We keep the eigenvector that corresponds to the lowest eigenvalue λ, since we are looking for the ground state, and reshape it back into a tensor that updates the current site, this is illustrated in Fig. 2.11.

The DMRG algorithm can thus be summarized by the following:

- start with a random MPS,
- optimize the MPS matrices by the procedure described above,
- iteratively repeat the procedurex along the MPS.

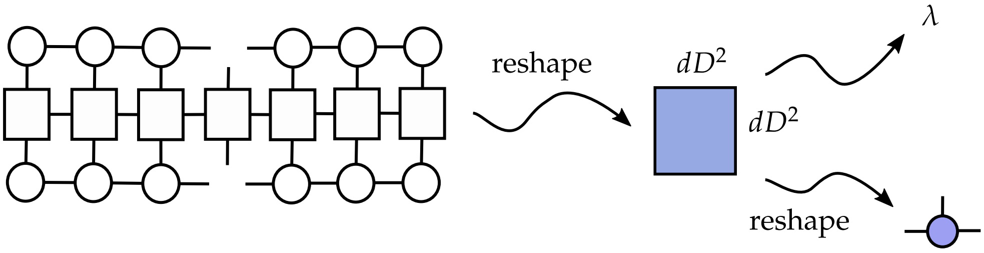

Figure 2.11: The local Hamiltonian tensor is reshaped into a matrix of dimension $dD^2 \times dD^2$ which is diagonalized. The diagonalization yields an eigenvalue λ and an eigenvector that is reshaped back into tensor form.

The quality of the MPS ground state crucially depends on the bond dimension and number of swipes along the MPS. We can think of the bond dimension as a parameter that controls the amount of correlation that can be represented with a MPS. We will see in chapter 3 that a surprisingly large bond dimension of 200 is needed to capture long ranged correlation phenomena such as the Kondo effect. Local quantities such as occupation numbers can be captured by MPS with a bond dimension of order 20.

The energy expectation value decreases with the number of swipes, though we observed that sufficient convergence is reached after about 5 swipes. We want to emphasize that bond dimension rather than number of swipes determines the quality of the ground state MPS that is obtained with DMRG. A thorough review of the DMRG can be found in Ref. [16] which includes all the mathematical details.

2.3.1 Numerical Renormalization Group in Matrix Product State language

We have seen that the MPS language offers a compact and computationally efficient representation of states and operators in 1D systems. Furthermore, mathematical manipulations such as expectation values have a simple and intuitive graphical representation. This motivates us to translate the ideas presented in the NRG into the language of MPS which will allow us to calculate the excitation spectrum of quantum impurity problems. Even though Wilson's NRG and White's DMRG might seem very different on the surface they turn out to be closely connected. To understand this, let us elaborate on the different nature of the RG step in NRG and DMRG.

The RG step in the NRG method is explicit in the sense that at every iteration only the low lying energy states are kept, the DMRG formulated in MPS language however only implicitly assumes RG steps. Rewriting a quantum state as a MPS, as presented in section 2.5, requires us to only keep low correlation states at every SVD step and therefore implicitly assumes a low correlation RG procedure. Though, it can be shown that for a sufficiently large bond dimension the DMRG is able to generate the same states as the NRG for quantum impurity models, this was first recognized by van Delft [18]. In fact, it can be shown that the states the NRG method yields can actually be rewritten in the form of MPS, see Ref. [18] for a thorough discussion.

Van Delfts MPS version of the NRG closely follows the spirt of DMRG. We start by calculating the ground state with DMRG by swiping along the chain and updating the matrixes. The ground state will now be used as a starting point for our excited state search, we can think of this as fixing a starting point in Hilbert space, see Fig. 2.12. Intuitively this should give us a better starting point than just starting with a random MPS which corresponds to starting at a random point in the subspace of MPS in the Hilbert space. We now perform one swipe from left to right along the chain, though this time we are not just keeping the lowest eigenvalue and corresponding eigenstate but rather the full spectrum of states that is obtained in the local diagonalization. If we recall Fig. 2.11, the set of eigenvalues λ that are obtained are the excitation energies for that site. What we notice is that this procedure only makes sense if the sites are probing different energy scales which means that just like in the NRG the Hamiltonian has to be behaved such that energy scales are separated within the Hamiltonian.

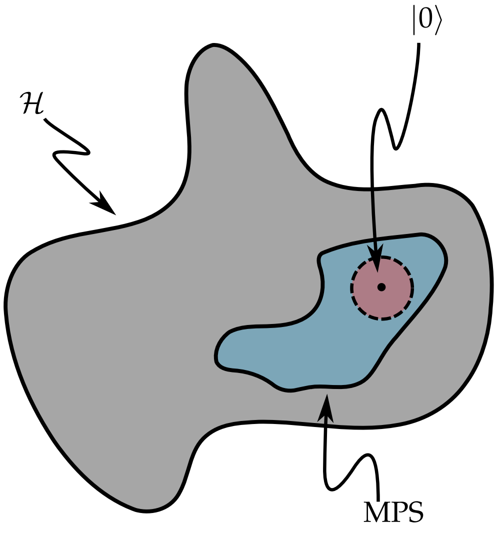

Figure 2.12: The ground state $|0\rangle$ yields a starting point in Hilbert space that allows to search for excited states. The dashed red circle characterizes a region that comprises states that describe similar physics as the ground state.

2.4 Quantum Information Approach

Quantum Information Theory has seen an explosion in popularity in the resent decades and has recently started diffusing into the Condensed Matter realms. We will use concepts of Quantum Information Theory to explore the entanglement details of our model. Let us start our discussion by introducing the main tool of all further analysis, the density matrix

$$\rho = \sum_{ij} p_{ij} \left|\psi_j\right\rangle \left\langle\psi_i\right| . \tag{2.32}$$

The density matrix is a very elegant way of dealing with so called mixed states, a mixed state describes a statistical ensemble of the usual state vectors $|\psi_i\rangle$. This means that the system cannot simply be described by a single state vector, called a pure state, but rather an ensemble of states weighted with a probability p_{ij}. The purity is given by

$$\mathcal{P} = Tr(\rho^2) \tag{2.33}$$

and gives us a measure of how much information would be lost if we simply described the system with a single state vector $|\psi\rangle$. The purity ranges from 1, for a pure system, to $\frac{1}{N}$, where N is the number of states that are mixed. For our quantum impurity problem at hand, this introduces the ability to study the mixing between the impurity and the conduction electrons. The density matrix of the impurity is obtained by tracing over the environment, the conduction electrons

$$\rho_{\text{imp}} = Tr_{\text{env}}(\rho). \tag{2.34}$$

In MPS language this simply means that the physical legs of the conduction electron sites in the density matrix MPO have to be contracted, as shown in Fig. 2.13.

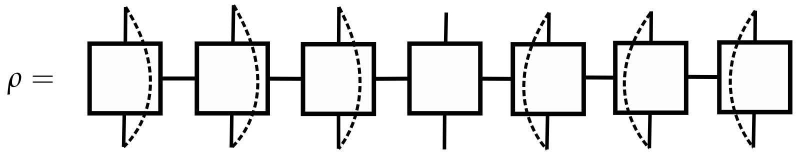

Figure 2.13: The reduced density matrix is obtained by tracing out the environment which translates to connecting the physical legs of the conduction fermion sites of the density matrix MPO, indicated by the dashed lines.

For a impurity purity, $\mathcal{P}_{\text{imp}} = Tr(\rho_{\text{imp}})$, of 1 this means that the impurity is completely isolated from the environment. A purity $\mathcal{P}_{\text{imp}} < 1$ means that the impurity is entangled with the environment, the conduction electrons. This allows to specifically target the Kondo singlet formation which is characterized by an entanglement between the conduction electrons and the impurity spin.

Chapter 3

Results

It this chapter of the thesis we will finally put the methods that were developed in the previous chapter to use. The goal is to thoroughly investigate the entanglement between the quantum dot and electronic cavity and possible competition with Kondo type physics. We will first investigate the occupation properties of the dot and the electronic cavity to gain a first rudimentary understanding of the problem and estimate the possible parameter regime for entanglement. The entanglement will be studied further by looking at the correlation properties as well as the Quantum Information Theory approach, this will yield a surprising result for the Anderson Impurity model, where we encounter a phase transition in bond dimension. Appendix C encloses the results of our MPS-NRG procedure.

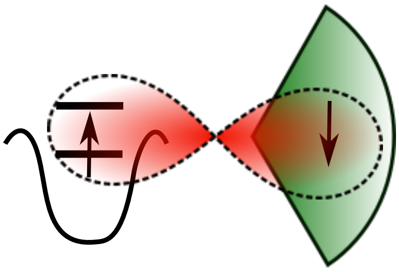

Figure 3.1: Quantum dot with two energy levels, energetically separated by the Coulomb repulsion U, entangled with one electron of the electronic cavity, indicated by the red cloud.

3.1 Occupation Properties

As a first step in our analysis we will investigate the ground state occupation properties of the quantum dot and the quantum dot coupled to an electronic cavity. To obtain the ground state we construct the Hamiltonian MPO of both models, following the approach introduced in section 2.2.4. The ground state in MPS form is calculated via DMRG, as presented in section 2.3. The dot is positioned at the zeroth site in the chain, coupling to the conduction sites via V, as shown in Fig. 1.3. After the ground state energy has converged we evaluate the total occupation expectation value at the dot

$$n_{\text{total}} = \langle 0| \, n_{d\uparrow} + n_{d\downarrow} \, |0\rangle \,, \tag{3.1}$$

while varying the on-site energy ε_d of the dot. The results of this calculation are shown in Fig. 3.2. To understand the physics behind the observed

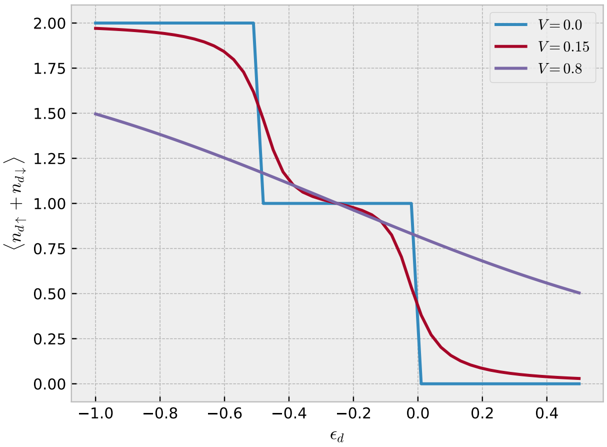

Figure 3.2: Total occupation of the quantum dot as a function of the on-site energy ε_d for different bath couplings V. The Coulomb repulsion is set to $U = \frac{1}{2}$, thus setting the single occupation region to $[-\frac{1}{2}, 0]$ for $V = 0$. The occupation curve is smoothed out for higher V. The results were obtained for a chain length of 40 and a bond dimension of $D = 40$.

phenomena, we first consider an isolated dot, $V = 0$. For a negative on-site energy ε_d the energy is minimized by occupying the dot with two electrons. Once we increase the on-site energy to the Coulomb repulsion, $-\varepsilon_d = -U$, the energy gain of putting in two electrons is overcome by the cost of the Coulomb repulsion, thus giving a region of single particle occupation. Once the on-site energy becomes positive, adding particles simply increases the energy, thus we see that the occupation drops to zero. The situation becomes more interesting once we switch on the coupling to the conduction electrons V. This introduces quantum tunneling from the dot to the bath and the other way around which causes the jumps between the three different occupation regions to smooth out. Fig. 3.3 shows how we can picture these three different situations, ε_F denotes the Fermi energy.

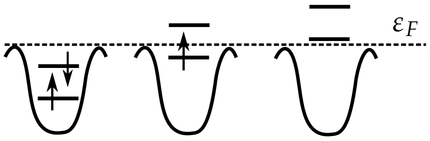

Figure 3.3: Three possible configurations of the quantum dot, with double spin degeneracy for the doubly and single occupied case.

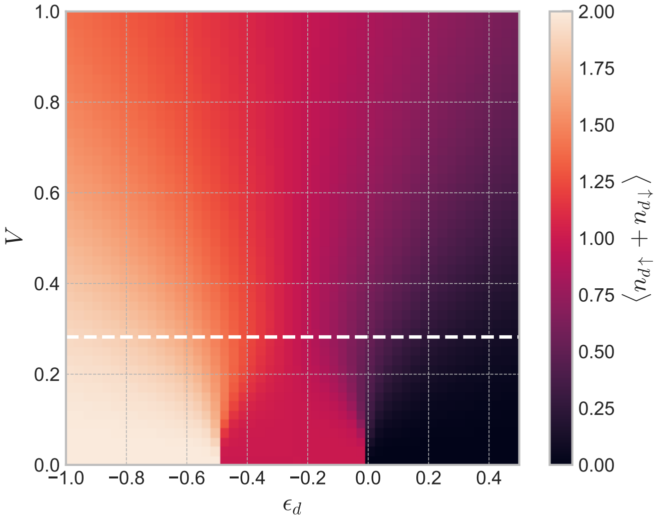

Figure 3.4: Total dot occupation $\langle n_{d\uparrow} + n_{d_\downarrow} \rangle$ as a function of bath coupling V and on-site energy ε_d. We can see the double (white), single (red) and unoccupied (black) configurations crossing over to a smoothed out region of occupation slightly above and below one. The Coulomb interaction is set to $U = \frac{1}{2}$. The white dashed lines marks the transition to local momentum formation.

We can see in Fig. 3.2 that there seems to be a transition point for a certain bath coupling V where the single particle occupation region vanishes. To further investigate how V influences the occupation we carried out the same calculation both as a function of ε_d and V. Fig 3.4 shows how the competition of the on-site energy and V, essentially the potential energy and kinetic energy, influences the total occupation. We can see that for small V there are three distinct integer occupation regions, once V is increased further the single occupation region disappears. A strong V means that electrons are hopping on and off both energy levels even if they lie above the Fermi surface. For example, in the situation where the energy level $\varepsilon_d + U$ is slightly above the Fermi energy, electrons keep hopping onto the upper layer, thus increasing the occupation expectation value. This transition was analytically analysed by Anderson [27], as discussed in section 1.1.4. He determined the condition for single particle occupation to be given by

$$V \ll \sqrt{\frac{\varepsilon_d + U}{\pi\rho}}. \tag{3.2}$$

We can see that our numerical results in Fig. 3.4 replicate the analytical transition line marked by the white dashed line.

Now, let us investigate how adding an electronic cavity, a single controllable energy level, changes the observed properties. The dot and the electronic cavity are now positioned in the middle of the chain, coupled via Ω and coupling to the right and left lead via t_L and t_R, as illustrated in Fig. 1.5.

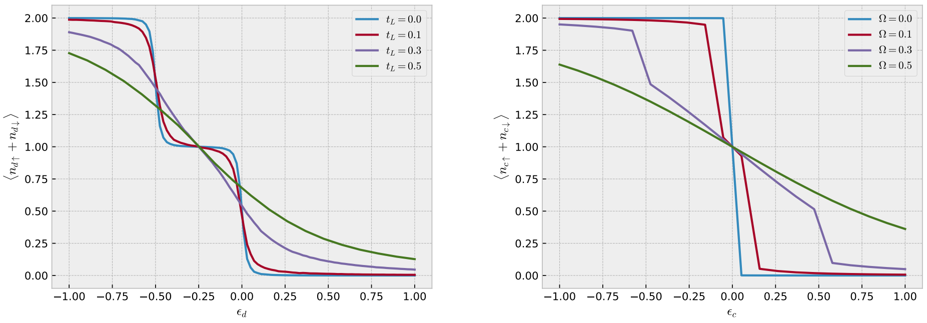

(a) Total dot occupation

(b) Total electronic cavity occupation

Figure 3.5: Total occupation of the quantum dot and electronic cavity as a function of on-site energy $\varepsilon_{d,c}$. The dot occupation was calculated for different lead couplings t_L while keeping the coupling to the cavity constant $\Omega = 0.1$. The cavity occupation was calculated for different dot cavity couplings Ω while keeping the lead coupling constant $t_{L,R} = 0.01$. The results were obtained for a chain length of 40 and a bond dimension of $D = 40$.

We first fix the coupling between the dot and the cavity and analyse the occupation properties of the dot in the dot-cavity system. Fig. 3.5a shows that the dot occupation is largely unaffected and we observe the same occupation curve as for a simple dot. As a next step, we set the dot energy to the single particle occupation region, $\varepsilon_d = -\frac{U}{2}$, and look at how the occupation curve of the cavity is affected by changes in the dot-cavity coupling. We can see in Fig. 3.5b that even though there is no Coulomb repulsion in the electronic cavity, the emergence of a single particle occupation region with increasing dot-cavity coupling Ω. This means that the dot and the electronic cavity seem to be entangled, therefore causing the electronic cavity to exhibit similar occupation properties as the dot.

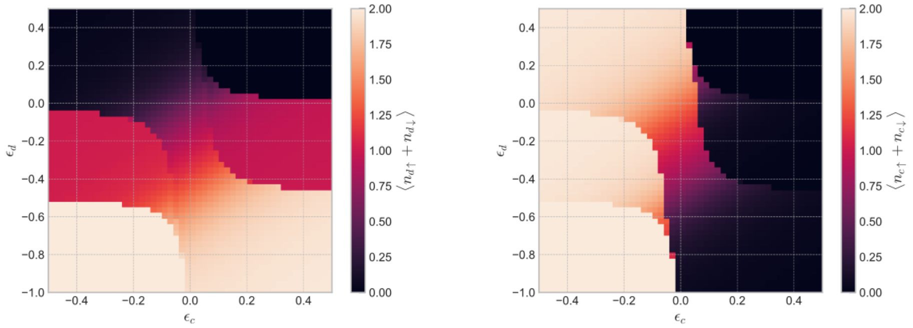

(a) Total dot occupation

(b) Total electronic cavity occupation

Figure 3.6: Total occupation of the quantum dot and electronic cavity for bath couplings $t_{L,R} = 0.01$ and dot-cavity coupling $\Omega = 0.1$ as a function of dot energy ε_d and electronic cavity energy ε_c.

To further understand this interplay between the dot on-site energy ε_d and the electronic cavity on-site energy ε_c we fixed the dot-cavity coupling and the coupling to the conduction electrons and calculated the occupation as a function of ε_d and ε_c. The results are shown in Fig. 3.6a and Fig. 3.6b. We can see that the dot-cavity coupling causes the emergence of a single particle occupation region in the dot and cavity.

Fig. 3.7 shows the total occupation of the dot-cavity system, where we can observe five different occupation regions. The occupation is indicated by (n_d, n_c), we can see that it ranges from an unoccupied dot-cavity system, $(0,0)$, to double occupation in dot and cavity, $(2,2)$. We can see that jump lines in the dot and electronic cavity occupation correspond to a change in the total occupation number. Going along the diagonal we can see how the occupation weight smoothly transitions from the cavity, $(0,2)$, to the dot, $(1,1)$ and $(2,1)$ without any change in the total occupation.

To study the entanglement between dot and electronic cavity we take a look at Fig. 3.6b and 3.7 we see that for $\varepsilon_d = -\frac{U}{2}$ the electronic cavity exhibits single particle occupation even though the on site energy ε_c is above the Fermi energy. This can only be energetically favourable if the electron in the

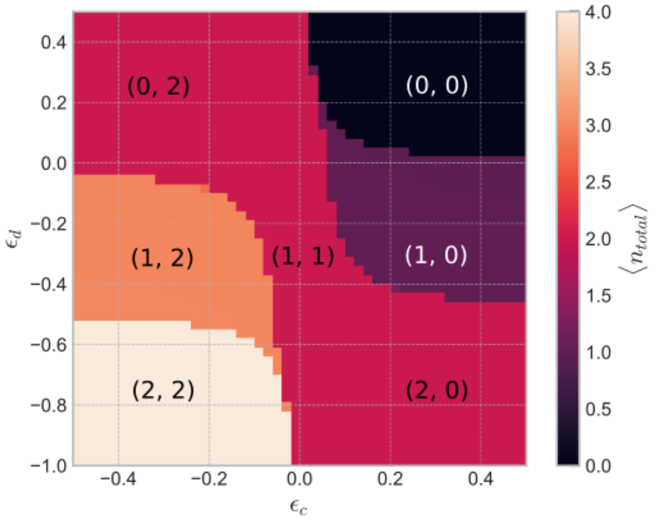

Figure 3.7: Total occupation of the dot cavity system $\langle n_{d\uparrow} + n_{d\downarrow} + n_{c\uparrow} + n_{c\downarrow} \rangle$ as a function of on site energies $\varepsilon_{d,c}$. The dot and cavity occupation is marked by (n_d, n_c). The couplings were fixed to $t_{L,R} = 0.01$ and $\Omega = 0.1$.

dot and electronic cavity form a singlet or triplet.

3.1.1 Correlation Properties

To further investigate this claim, we take a look at the dot-cavity occupation correlation

$$corr = \frac{\langle n_{d\uparrow} n_{c\downarrow} \rangle - \langle n_{d\uparrow} \rangle \langle n_{c\downarrow} \rangle}{\sigma_{n_{d\uparrow}} \sigma_{n_{c\downarrow}}} + \frac{\langle n_{d\downarrow} n_{c\uparrow} \rangle - \langle n_{d\downarrow} \rangle \langle n_{c\uparrow} \rangle}{\sigma_{n_{d\downarrow}} \sigma_{n_{c\uparrow}}}, \tag{3.3}$$

where $\sigma_X = \sqrt{\langle X^2 \rangle - \langle X \rangle \langle X \rangle}$ is the standard deviation of the occupation. The correlation ranges form -1 to 1, where 1 indicates that the spin orientation of the dot and electronic cavity are opposites. A correlation of 0 means that the spin orientations are independent of each other and randomly distributed. Parallel spins will exhibit negative correlation, because our correlation is defined as the anti parallel spin correlation.

We can clearly see in Fig. 3.8 that in the single occupation region of the dot and electronic cavity their spins form a singlet-triplet state,

$$\begin{aligned} |0\rangle = \alpha \big[\, |\uparrow_d \downarrow_c\rangle + |\downarrow_d \uparrow_c\rangle \, \big] \qquad (3.4) \\ + \beta \big[\, |\uparrow_d \downarrow_c\rangle - |\uparrow_d \downarrow_c\rangle \, \big], \qquad (3.5) \end{aligned}$$

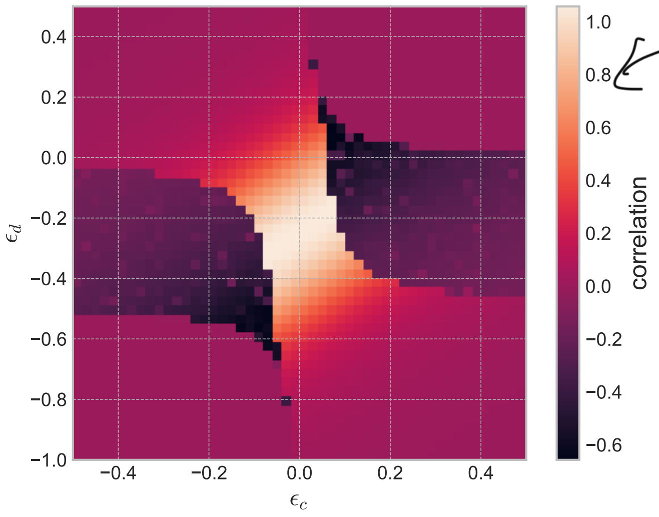

scan for diferent $|\Omega|$

Figure 3.8: Dot-cavity anti parallel spin orientation occupation number correlation as a function of dot energy ε_d and electronic cavity energy ε_c. The couplings were fixed to $t_{L,R} = 0.01$ and $\Omega = 0.1$.

with opposite spin directions, indicated by a correlation of one. The negative correlation region is the region where dot and electronic cavity occupation have a tail of single particle occupation, this indicates that the dot and electronic cavity electron pair up to form just a triplet,

$$|0\rangle = \alpha \left|\uparrow_d \uparrow_c\right\rangle + \beta \left|\downarrow_d \downarrow_c\right\rangle . \tag{3.6}$$

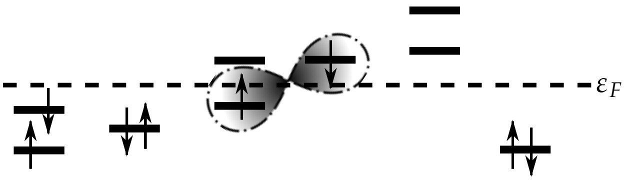

Figure 3.9: Three distinct dot-cavity configurations with two lines representing the two energy layers, separated by the Coulomb repulsion U. Single solid lines are the electronic cavity energies. The dashed line is the Fermi surface ε_F. The cloud in the middle symbolizes the singlet-triplet state formed by the dot and electronic cavity electron.

In Fig. 3.9 we see an example of three distinct situations. We can see that single occupied dot and electronic cavity form a singlet-triplet state, indicated by the cloud in the middle. In the left situation both dot and electronic cavity have double occupation but do not exhibit any entanglement features. The right situation trivially has no entanglement features since there is no electron in the dot to pair with the electronic cavity electrons. Our claims about the entanglement between dot and electronic cavity will be investigated further in section 3.2.

3.2 Quantum Information Approach

The occupation properties of the ground state for both the dot and dot-cavity have provided us with great insights into their entanglement features, though we were not able to extract much information about Kondo physics. This section aims at resolving the shortcomings of the previous sections, specifically targeting Kondo physics, the entanglement with the conduction electrons. We will use the Quantum Information approach presented in section 2.4 to extract the purity of the Anderson Impurity and quantum dot-cavity which provides a measurement of the entanglement with the conduction electrons.

3.2.1 Purity flow

First, let us remind ourself of the Kondo effect, presented in section 1.1.5. For temperatures below the Kondo temperature T_K the impurity spin will form a singlet with a collection of conduction electrons. Fermions around the Fermi surface continuously scatter with the impurity spin, causing a peak in the density of states. The question we want to answer is in what parameter regime a Kondo singlet forms and how it is entangled to the environment. To do that, we build the ground state density matrix of the entire system by calculating the outer product of the ground state $|0\rangle$ with itself

$$\rho_0 = |0\rangle \langle 0| \,. \tag{3.7}$$

To investigate the impurity, we trace out the environment, as described in section 2.4. The purity of the impurity is calculated by tracing over the square of the reduced density matrix

$$\mathcal{P} = Tr_{\text{env}}(\rho^2_{0,\text{imp}}). \tag{3.8}$$

To gauge this method we first calculated the purity as a function of chain length and compared the DMRG results with exact diagonalization (ED). Longer chains give higher energy resolution around the Fermi energy, where we expect conduction electrons to Kondo scatter with the impurity spin.

The results are shown in Fig. 3.10a and Fig. 3.10b . The purity exhibits features very similar to the NRG and we will call the change of the purity as a function of chain length purity flow and use the term fixed point for a converged purity.

We observe in Fig 3.10a and Fig. 3.10b that a fairly low bond dimension of 5 in the DMRG is needed to accurately capture the physics of a fixed point. This indicates that the correlations are low for pure and fully mixed states, once the fixed point is reached. A pure state means that the electrons in the dot do not interact with the environment and there is thus no correlation which allows us to use a very low bond dimension. The situation for a fully mixed state is more interesting, one might expect the dot electrons to mix with fermions from all along the chain, thus giving a fairly large correlation which would need a higher bond dimension to capture. Though apparently the numerical calculations indicate that a bond dimension as low as 5 is accurate enough to match the ED results. However, this will turn out to not to be the whole story, as we will see in the next section. Though, before that let us make some more comments about the ED vs DMRG results.

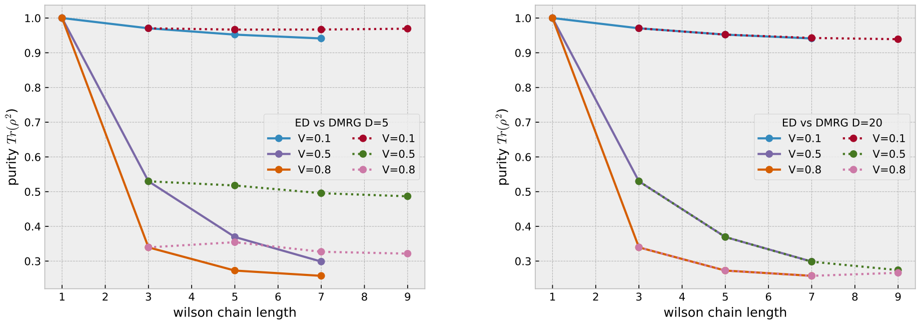

(a) Purity flow for $D = 5$

(b) Purity flow for $D = 20$

Figure 3.10: Comparison of the purity flow of the Anderson Impurity model with $\varepsilon_d = -\frac{U}{2}$ and $U = \frac{1}{2}$ between ED (solid lines) and DMRG (dashed lines) for different bath couplings V. The purity was calculated as a function of Wilson chain length. Once a fixed point is reached a low bond dimension of 5 is sufficient to match the ED results. A bond dimension of 20 is needed to capture the longer ranged correlations away from a fixed point.

So it seems like our method agrees with ED for a bond dimension above 20 and we therefore went on to calculate the purity flow for longer chain lengths to see how the flow is affected by the dot bath coupling V. We can see in Fig. 3.11 that the transition to the fixed point is happening earlier in the chain for higher bath coupling V. This makes intuitive sense since

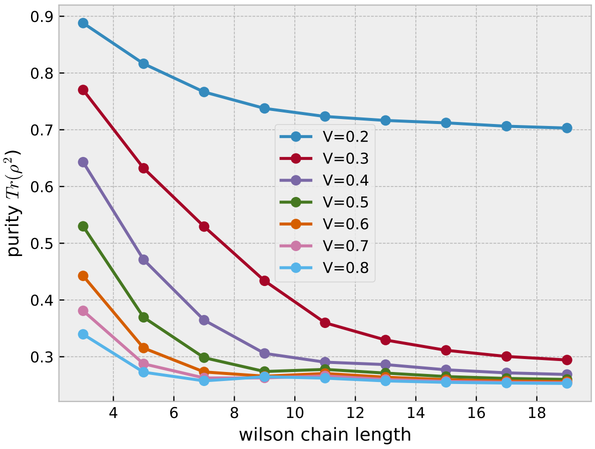

Figure 3.11: Purity flow of the Anderson Impurity model with $\varepsilon_d = -\frac{U}{2}$ and $U = \frac{1}{2}$ for different bath couplings V. A bond dimension of $D = 20$ was used for the calculation.

higher V means that the impurity spin interacts stronger with the conduction electrons and thus mixes with more states which decreases the purity.

Though, the deciding test of our method is whether we can see the Kondo singlet formation. As discussed in section 1.1.5 Kondo singlet formation happens in the single particle occupation region of the Anderson Impurity model. The impurity spin will entangle with a collection of conduction electrons and form a singlet state which is characterized by a purity of $\frac{1}{2}$, see Appendix B for a derivation of this result.

3.2.2 Kondo Singlet formation in the Anderson Impurity model

We therefore went on to set the parameters to the single particle occupation region and analysed the purity as a function of chain length and bond dimension. We can see in Fig. 3.12a that the purity converges for a chain length of around 15, though it is high above the expected singlet purity of $\frac{1}{2}$, so it seems like the bond dimension might be too low to capture the high correlation Kondo singlet formation. Thus, we went on to calculate the purity as a function of bond dimension which yields a rather surprising result. We can see in Fig. 3.12b that the purity decreases with bond dimension until something like a phase transition is happening and the purity stays constant after a rapid decrease. This is in fact the Kondo singlet formation!

It looks like the bond dimension plays the role of an order parameter which determines the transition from non-Kondo physics to a Kondo singlet forma-

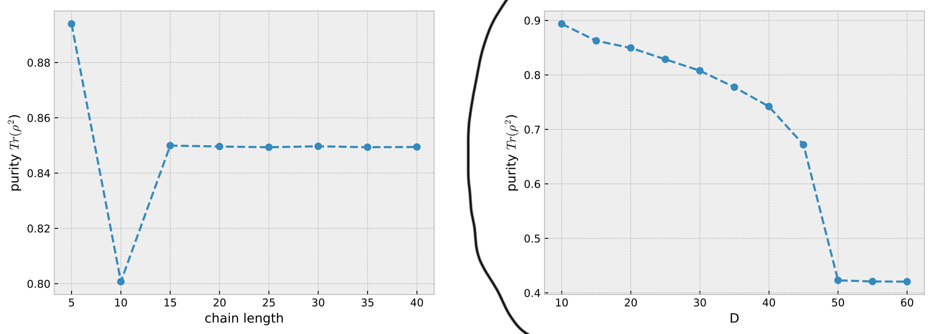

(a) Purity as a function chain length

(b) Purity as a function of D

$\mathrm{Tr}\rho\log\rho$
vs
$\mathrm{Tr}\rho^2$

Figure 3.12: Purity of the Anderson Impurity in the single occupation region, $\varepsilon_d = -\frac{U}{2}$ and $V = 0.15$ as a function of chain length and bond dimension D with a Coulomb interaction $U = \frac{1}{2}$. We can see that convergence is reached for a length of 15 and a bond dimension of $D = 50$.

tion. Kondo singlet formation means that the effective spin of the conduction electrons entangles with the impurity spin and forms a singlet. However, if the bond dimension is too low, the MPS is not able to capture the singlet formation and it will simply yield a non-singlet mixed state.

The position of the effective conduction spin depends on the bath coupling V, for example low V means that mainly fermions around the Fermi energy interact with the impurity spin. Due to the log-discretization of the conduction chain this translates to a possible singlet formation with an effective conduction spin that is positioned at a high chain index. If the provided bond dimension is too low to capture correlations up to that site, no Kondo singlet formation will be observed.

Fig. 3.13 shows this interplay between bath coupling V and bond dimension. We can see that a surprisingly high bond dimension of 200 is needed to capture Kondo singlet formation in the low V region. For $V = 0$ the purity is trivially 1 since a completely decoupled impurity cannot entangle with anything and it can only yield a pure state. Additionally, we can observe in Fig. 3.13 how the purity smoothly crosses over from a Kondo singlet to a fully mixed state of purity $\frac{1}{4}$ for higher V. A fully mixed state is characterized by all possible states being equally mixed giving a purity of $\frac{1}{N}$ where N is the number of states, see section 2.4. This means that all 4 possible states, the two doubly-degenerate energy levels ε_d and $\varepsilon_d + U$, equally mix with the conduction electrons.

We tried to obtain a scaling law from Fig. 3.13 for the critical bond dimension D_{crit} as a function of bath coupling V, the result is shown in Fig. 3.13. We

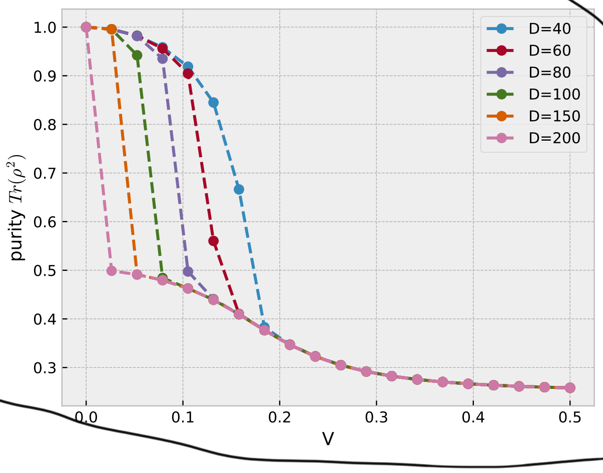

Figure 3.13: Purity of the Anderson Impurity model for $\varepsilon_d = -\frac{U}{2}$ and $U = \frac{1}{2}$ as a function of V for different bond dimensions D. The chain length was set to 20.

can see that the critical bond dimension oscillates around

$$D_{\text{crit}} \propto \frac{1}{V}, \tag{3.9}$$

though the data is not sufficient to determine a definitive scaling law and more analysis is needed. The oscillations could be due to finite size effects, so a longer chain length might improve the results. Another possible reason is that the effective Kondo spin might be positioned at an integer site position in the chain and can thus only jump between sites.

A thorough analysis of the scaling of the critical bond dimension D_{crit} could possibly allow to determine the position of the effective conduction electron spin in the chain.

Now that we know the parameter regime for Kondo single formation, we extend our analysis to the whole range of on-site energies ε_d, not just the single particle occupation region. Fig. 3.15a shows the result for a bond dimension of 40, which is clearly not enough to capture Kondo singlet formation in the single particle occupation region. In Fig. 3.15b we can see that the situation changes when a sufficient bond dimension of 200 is used. We can clearly observe a purity of $\frac{1}{2}$ in the entire single particle occupation region, though we notice that for some data points in the low V region a bond dimension of 200 is still not enough to capture the Kondo singlet formation. The non and double occupied regions smoothly cross over from a pure state to a fully mixed state for higher bath coupling V, this remains unaffected by the change in bond dimension.

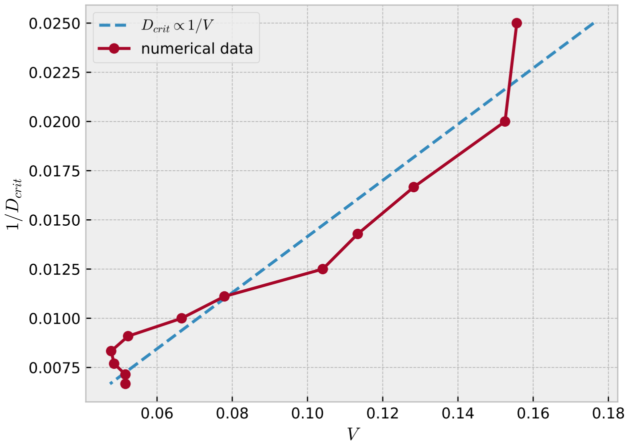

Figure 3.14: Inverse critical bond dimension $1/D_{crit}$ for Kondo single formation as a function of bath coupling V. The scaling was analysed for a purity of 0.7 for the Anderson Impurity model with $\varepsilon_d = -\frac{U}{2}$ and $U = \frac{1}{2}$.

The remaining question is why there seems to be a Kondo singlet formation in the low bond dimension case for $\varepsilon_d = 0$ and $\varepsilon_d = -U$, marked by the white arrows in Fig. 3.15a. This can in fact be explained by looking at the Kondo temperature in Eq. (1.21), we notice that the Kondo temperature has a maximum for $\varepsilon_d = -U$ and $\varepsilon_d = 0$ which means that the effective conduction spin is positioned close to the impurity in the chain. These two on-site energies are thus the two energies where Kondo physics is fully probed for the lowest bond dimension.

D=40

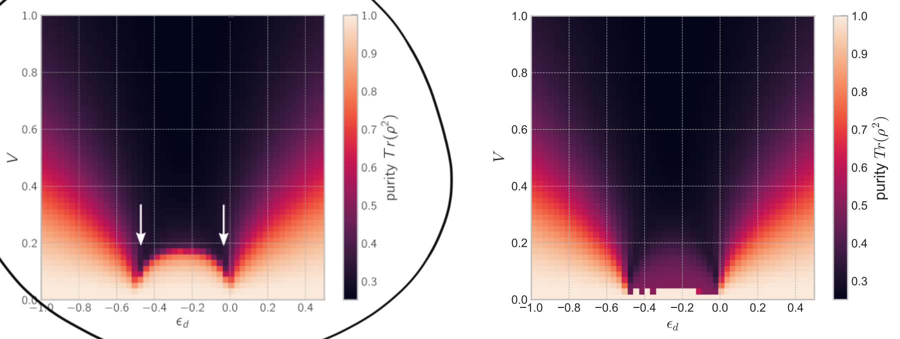

(a) Purity heatmap for $D = 40$ (b) Purity heatmap for $D = 200$

Figure 3.15: Purity of the Anderson Impurity model as a function of V and on-site energy ε_d with a Coulomb interaction $U = \frac{1}{2}$ for a bond dimension $D = 40$ and $D = 200$ and chain length of 40 and 20 respectively. White arrows indicate a cross over to a Kondo singlet formation, in the low bond dimension case.

3.2.3 Purity of a Quantum Dot coupled to an Electronic Cavity

We have seen that our method is able to accurately capture Kondo singlet formation for bond dimensions above the critical bond dimension D_{crit}, we therefore proceeded to repeat the Quantum Information approach for the dot-cavity system. Though, due to computational limitations we were only able to perform this calculation for the high coupling limit $\Omega \gg t_{L,R}$ where the entanglement is dominated by a singlet-triplet formation between dot and electronic cavity and a bond dimension of 40 is sufficient.

Fig. 3.16 shows that the dot-cavity system forms a pure state in the single particle occupation $(1, 1)$ region of the dot and electronic cavity. Together with the previous correlation result, this confirms that the dot and electronic cavity indeed form a singlet-triplet. More interesting though is the fact that the tails in the $(0, 1)$ and $(1, 0)$ occupation region, where we observed negative correlation, yield a purity of one too which gives strong evidence for our claim that the dot and electronic cavity form a pure triplet in that region. We can also see that the dot-cavity system trivially forms a pure state for $(2, 2)$-occupation and $(0, 0)$-occupation, double occupied dot $(2, 0)$ and electronic cavity $(0, 2)$ fully mix with the environment.

$D = 40 \xrightarrow{?} D = 200$

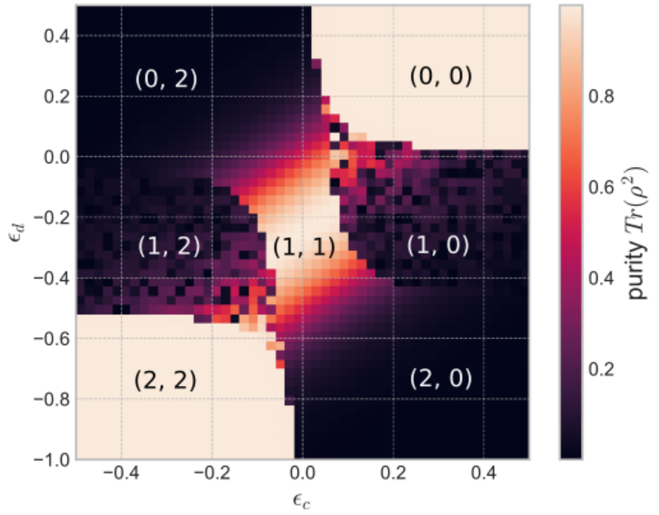

Figure 3.16: Purity of the dot-cavity system as a function of dot energy ε_d and electronic cavity energy ε_c. The occupation of the dot-cavity system is indicated by (n_d, n_c). The results were obtained for a chain length of 40 and bond dimension $\boxed{D = 40.}$

Also plot: ρ^2 of only the dot

$D = 40$ & 200

$\Omega, t = (0.01, 0.1)$ & $(0.1, 0.01)$

& each time: $Tr\rho_{dot}^2$ & $Tr\rho_{dot\text{-}cav}^2$

Chapter 4

Conclusion and Outlook

To conclude this thesis we will first summarize our work and show its connection to the current stage of research on the matter. Furthermore, we will highlight the great potential of our technique for possible future work and provide an outlook for the various directions the research could be extended to.

Classical computation has pushed humanity into the Digital Age, our economies have shifted from classical industry to information based technology and computers have become an integral part of our lives, though it seems like classical computation is slowly reaching its full potential. While Moore's law [39] is crumbling a new technology is rising up on the horizon, quantum computing is praised as the antidote to a slow down in technological development. Building a quantum computer is a technologically challenging endeavour and many different technologies are competing for the pole position. In the first chapter we presented how quantum dots coupled to electronic cavities could offer a scalable and robust physical realization of qubits, the fundamental computation unit of quantum computers. Quantum dots and the dot-cavity system additionally offers experimentalists the possibility to specifically target fascinating quantum many-body effects such as the Kondo singlet formation. Even though the Kondo effect was first experimentally observed in 1934 [15], for impurities in metals, it is only now that the effect can be studied on a single impurity due to the experimental realization of quantum dots [2]. This led to to a renaissance in theoretical research on Kondo impurity systems.

After introducing the model we developed a variety of MPS based tools in the second chapter that allowed us to study the occupation and entanglement properties of the dot and electronic cavity. The results of our numerical analysis were presented in the third chapter. Initially, the aim of our work was to get a better understanding of the entanglement properties of the dot-cavity system, though we discovered something more striking. We saw that there seems to be a critical bond dimension for Kondo singlet formation. The transition between non-Kondo and Kondo exhibits features very similar to a phase transition. To our knowledge this might be a novel feature and offers great opportunities for further investigation. During the development of the KPM, as presented in Appendix D, we noticed a break down of the method below a certain bond dimension, in retrospective this could be the same transition we encountered with the Quantum Information approach. Therefore, this could be a general feature of MPS. The next possible step is to investigate if the same phase transition can be observed in NRG, since MPS and NRG yield similar states for quantum impurity models [18].

We saw that Kondo singlet formation in the low bath coupling V region is only observed for a very large bond dimension of order 200. A significantly lower bond dimension could possibly be used by unfolding the chain. Since the spin degrees of freedom only couple at the impurity in the Coulomb term, this allows to position the spin up and down conduction sites to the left and right of the impurity. This increases the length of the chain but significantly reduces the bond dimension at same time [18]. An unfolding of the chain could thus possibly allow to access the phase dimension for a fairly low bond dimension of order 20.

Additionally, we were able to show that the dot and electronic cavity can be tuned such that they are both occupied by a single electron. By investigating the correlation and purity properties, we saw that the dot and electronic cavity form a singlet-triplet state which is in agreement with the experimental observations presented in Ref. [11, 12] as well as the theoretical results presented in Ref. [13, 14]. This remarkable result opens up the opportunity to study two quantum dots coupled via an electronic cavity. This has already been experimentally realized, as presented in Ref. [3, 4, 5], but is still lacking a thorough theoretical investigation. Our techniques can trivially be extended to provide new theoretical insights into the experimental data and possibly provides experimentalists with inspiration for new experiments.

The MPS-NRG technique, discussed in Appendix C, turned out to be mainly uncharted territory and provides great opportunities for further research as well. Apart from potentially offering a computationally superior technique for obtaining the spectral function and excitation spectra, it is also very interesting to explore classical RG properties such as fixed points within the MPS-language. Especially the RG flow next to a fixed point could be a very interesting property to be studied with MPS.

All in all, this work should be understood as laying the groundwork for future investigations on quantum impurity Kondo physics. Especially the results of the Quantum Information approach for the Anderson Impurity are rather striking and offer numerous future research opportunities.

Appendix A

Fermionic operators

We present the fermionic operator matrices in the spin full occupation basis, given by $\{|0\rangle, |\uparrow\rangle, |\downarrow\rangle, |\uparrow\downarrow\rangle\}$. The fermionic anti-commutation relations are taken care of by a Jordan Wigner transformation, see Ref. [40] for more information.

$$c_\uparrow^\dagger = \begin{bmatrix} 0 & 0 & 0 & 0 \\ 1 & 0 & 0 & 0 \\ 0 & 0 & 0 & 0 \\ 0 & 0 & 1 & 0 \end{bmatrix} \qquad c_\downarrow^\dagger = \begin{bmatrix} 0 & 0 & 0 & 0 \\ 0 & 0 & 0 & 0 \\ 1 & 0 & 0 & 0 \\ 0 & 1 & 0 & 0 \end{bmatrix} \tag{A.1}$$

$$c_\uparrow = \begin{bmatrix} 0 & 1 & 0 & 0 \\ 0 & 0 & 0 & 0 \\ 0 & 0 & 0 & 1 \\ 0 & 0 & 0 & 0 \end{bmatrix} \qquad c_\downarrow = \begin{bmatrix} 0 & 0 & 1 & 0 \\ 0 & 0 & 0 & 1 \\ 0 & 0 & 0 & 0 \\ 0 & 0 & 0 & 0 \end{bmatrix} \tag{A.2}$$

Appendix B

Purity of a Singlet state

Let us take the Anderson Impurity model as an example and label the impurity state with L and the collective conduction electron spin with R. The singlet state can thus be written as

$$|\psi\rangle = \frac{1}{\sqrt{2}}\big[\, |\uparrow_L \downarrow_R\rangle - |\downarrow_L \uparrow_R\rangle \,\big]. \tag{B.1}$$

We calculate the density matrix ρ by taking the outer product

$$\begin{aligned} \rho &= |\psi\rangle \langle\psi| && \text{(B.2)} \\ &= \frac{1}{2} |\uparrow_L \downarrow_R\rangle \langle\uparrow_L \downarrow_R| - \frac{1}{2} |\uparrow_L \downarrow_R\rangle \langle\downarrow_L \uparrow_R| && \text{(B.3)} \\ &- \frac{1}{2} |\downarrow_L \uparrow_R\rangle \langle\uparrow_L \downarrow_R| + \frac{1}{2} |\downarrow_L \uparrow_R\rangle \langle\downarrow_L \uparrow_R|, && \text{(B.4)} \end{aligned}$$

and partially trace out the conduction electrons R by writing

$$\begin{aligned} \rho_L &= Tr_R(\rho) && \text{(B.5)} \\ &= \langle\uparrow_R| \rho |\uparrow_R\rangle + \langle\downarrow_R| \rho |\downarrow_R\rangle && \text{(B.6)} \\ &= \frac{1}{2} |\uparrow_L\rangle \langle\uparrow_L| + \frac{1}{2} |\downarrow_L\rangle \langle\downarrow_L|. && \text{(B.7)} \end{aligned}$$

Which means that the purity of the impurity $\mathcal{P} = Tr(\rho_L^2)$ is simply $\frac{1}{2}$.

Appendix C

Numerical Renormalization Group

This section discusses the results that were obtained for the MPS-NRG approach. Our original goal with this method was to translate the NRG approach for obtaining the spectral function into the MPS language, see Ref. [17]. It turned out that this is mainly uncharted territory and there are many open questions that have to be addressed to develop the method further. We will summarize the main results and discuss what went wrong and what could possibly be done to make it work. All results were only obtained for the Anderson Impurity model.

C.0.1 Renormalization Group Flow

We have seen in section 2.3.1 that the excitation spectrum of quantum impurity problems in the Wilson basis can be obtained by fully diagonalizing the local Hamiltonian matrix [18]. This is due to the log discretization of the conduction band which allows to probe an exponentially decaying energy scale $\propto \Lambda^{-n/2}$ for Wilson sites n.

The excitation energies, ε_n^r, with r labeling the excitation, are an approximate subset of the full spectrum of the Hamiltonian at energy scale $\propto \Lambda^{-n/2}$, this means that at the zeroth site the full spectrum is probed and all further sites probe a subset of energies closer to the lowest energy, the ground state. The RG flow can be visualized by rescaling the energies by the probed energy scale

$$\varepsilon_{n,\mathrm{rescaled}}^r = (\varepsilon_n^r - E_0)/\Lambda^{-n/2}, \tag{C.1}$$

as seen in Fig. C.1b.

Unfortunately, this result seems to disagree with the established NRG result in Ref. [41]. One would expect to see three distinct fixed points, starting with the free-orbital fixed point, crossing over to the local-momentum fixed point and finally crossing over to the strong-coupling fixed point, for the lowest lying energies, as mentioned in section 2.1.3. This feature is not as pronounced in our MPS-NRG scheme, though there seem to be three different regions, when considering the full spectrum. Due to the lack of a pronounced flow, we were not able to extract any more information, such as the Kondo temperature, from the RG flow.

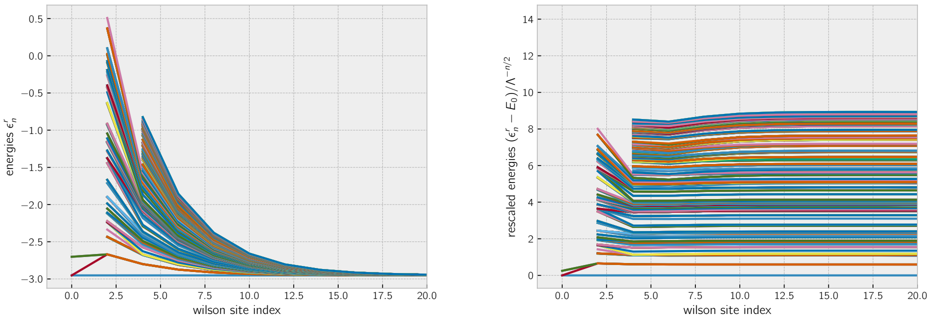

(a) Unscaled excitation energies

(b) Rescaled excitation energies

Figure C.1: Unscaled and rescaled excitation energies of the MPS-NRG scheme for the Anderson Impurity model as a function of the Wilson site index. Unscaled energies decay $\propto \Lambda^{-n/2}$ due to the log discretization of the conduction band. The bond dimension increases by a factor of d until it is truncated to D, therefore a lower number of eigen-energies is obtained for the first few sites. See Ref. 2.10 for details. The simulation parameters were $\Lambda = 2.0$, $D = 20$, $U = 0.5$, $V = 0.1$, $\varepsilon_d = -\frac{U}{2}$ and a chain length of 20.

C.0.2 No spectral function

Following Ref. [17] we went on to calculate the zero temperature spectral function

$$\begin{aligned} A_\sigma(\omega) \propto \sum_r |\langle r, n| \, d_\sigma \, |0\rangle|^2 \delta(\omega + (E_r - E_0)) \qquad \text{(C.2)} \\ + \sum_{r'} |\langle 0| \, d_\sigma \, |r', n\rangle|^2 \delta(\omega - (E_{r'} - E_0)) \qquad \text{(C.3)} \end{aligned}$$

given in the Lehmann representation. The state $|r, n\rangle$ is the r^{th} eigenvector corresponding to the n^{th} Wilson site. The problem with this approach is how to properly translate the calculation of the matrix elements into MPS language. The annihilation operator for the dot d_σ acting on the ground state $|0\rangle$ will simply give zero, in the single occupied case.

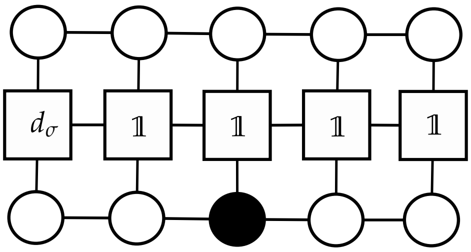

Figure C.2: Visualization of the matrix element $\langle r, n| \, d_\sigma \, |0\rangle$ in Eq. (C.2). The annihilation operator d_σ acts on the dot site. The black circle represents the state of the r$^{\text{th}}$ excitation on the n$^{\text{th}}$ Wilson site, $|r, n\rangle$.

This means that no matter what $|r, n\rangle$ is, the zero of the first site will just be contracted with the rest to give an overall zero matrix element, as seen in Fig. C.2. This issue does not arise in the classical NRG variation because a truncated number of the excitation energies is kept at every iteration which means that the site n also carries information about the excitations for sites $< n$. The MPS-NRG variation, proposed by Ref. [18], however, only caries the ground state information of previous sites. This issue could possibly be resolved by carrying those matrix elements on the first site that are non zero as a left environment in the evaluation of the matrix element. Though, this has not been tried yet.

Appendix D

Kernel Polynomial Method

Another quantity of great interest in Condensed Matter and for our problem at hand is the spectral function. To motivate its importance, let us take a look at the formal definition of the correlator

$$G(t) = \langle 0| \, d(t) d^\dagger(0) \, |0\rangle \, . \tag{D.1}$$

This tells us that we are adding a fermion with $d^\dagger(0)$ to the ground state $|0\rangle$ and removing it at a later time t with $d(t)$ and compare that quantity to the original ground state. If we imagine our Anderson Impurity this translates to adding a fermion to the impurity, letting the system sit for a time t, removing the fermion and looking at what has changed. We can imagine that the coupling to the bath $V_{\vec{k}}$ causes fermions to hop in or leak out and therefore $G(t)$ provides us with a measurement of how much interaction is happening. The spectral function is now defined as the Fourier transformation of the correlator

$$\begin{aligned} A(\omega) &= \int \frac{dt}{2\pi} e^{i\omega t} G(t) && \text{(D.2)} \\ &= \langle 0| \, d \, \delta(\omega - \hat{H} + E_0) \, d^\dagger \, |0\rangle && \text{(D.3)} \end{aligned}$$

which means that instead of asking how much interaction is happening as a function of time we are asking how much interaction is happening as a function of frequency ω, see Ref. [20]. With some intuition, we can already anticipate what this means for the Anderson Impurity model: we expect a high value around the Fermi energy, where the Kondo resonance is happening and two peaks around ε_d and $\varepsilon_d + U$ where fermions are jumping on and off the available energy levels in the impurity.

The delta function in Eq. (D.3) can be expanded in terms of Chebyshev polynomials. The Chebyshev polynomials as defined by the recursion relations

$$T_{n+1}(x) = 2xT_n(x) - T_{n-1}(x), \tag{D.4}$$

with $T_0(x) = 1$ and $T_1(x) = x$. On the interval $I = [-1, 1]$ they form an orthonormal system and thus any smooth function on that interval can be expanded

$$f(x) = \frac{1}{\pi\sqrt{1-x^2}}\left[\mu_0 + 2\sum_{n=1}^{\infty} \mu_n T_n(x)\right], \tag{D.5}$$

with moments given by $\mu_n = \int_{-1}^{1} \mathrm{d}x\, f(x) T_n(x)$. Truncating the sum at N introduces some artificial oscillations, though they can be suppressed with appropriate broadening kernels replacing μ_n with $g_n\mu_n$, details about appropriate kernels can be found in Ref. [19].

D.0.1 Rescaling the spectrum

To expand the delta function in terms of Chebyshev polynomials we need to rescale the Hamiltonian such that its spectrum lies within the interval $I = [-1, 1]$. This is achieved by first calculating half of the spectrum width of the unscaled Hamiltonian H

$$W = \frac{E_{\max} - E_{\min}}{2}. \tag{D.6}$$

The ground state energy $E_{\min}$ is simply calculated via DMRG and $E_{\max}$ is obtained by calculating the ground state energy of $-H$. The rescaled Hamiltonian is simply given by

$$H \to \frac{H}{W}, \tag{D.7}$$

with new $E'_{\max}$ and $E'_{\min}$ now inside the interval $I = [-1, 1]$. Now we shift the spectrum such that $E'_{\max}$ and $E'_{\min}$ lie symmetrically around 0. This is done by writing

$$H \to H + (1 + \frac{E_{\max}}{W})\mathbb{1}. \tag{D.8}$$

Finally, as a safety measure we will scale the energies down to lie inside the interval $I = [-\varepsilon, \varepsilon]$ by writing

$$H \to \varepsilon H. \tag{D.9}$$

D.0.2 Chebychev expansion

After properly rescaling the Hamiltonian, we can go ahead and expand the delta function in Eq. (D.3) in terms of Chebychev polynomials,

$$\delta(\omega' - \hat{H}') = \frac{1}{\pi\sqrt{1-x^2}}\left[\mu_0 + 2\sum_{n=1}^{\infty}\mu_n T_n(x)\right]. \tag{D.10}$$

Using this expression and the recursion relation of the Chebychev polynomials Eq. (D.5), we can derive the moments μ_n

$$|t_0\rangle = d\,|0\rangle \quad |t_1\rangle = H\,|t_0\rangle \tag{D.11}$$

$$|t_n\rangle = 2H\,|t_{n-1}\rangle - |t_{n-2}\rangle\,, \tag{D.12}$$

$$\mu_n = \langle 0|\,d^\dagger\,|t_n\rangle\,, \tag{D.13}$$

where $|t_n\rangle$ are called Chebyshev vectors. Details of the implementation in MPS language can be found in Ref. [20]. Once the moments are calculated, they are used to express the delta function which allows to evaluate the spectral function, Eq. (D.3). The energy resolution of this method is proportional to $\frac{1}{N}$, where N is the number of calculated moments.

D.1 No Spectral function

Unfortunately, we were not able to obtain reasonable results with this method. Fig. D.1 shows the spectral function as a function of positive energy ω relative to the Fermi energy ε_F for the Anderson Impurity model. The on-site energy is set to the single particle occupation region $\varepsilon_d = -\frac{U}{2}$.

Kondo resonance is characterized by scattering of electrons around the Fermi energy with the impurity spin energetically positioned at $\pm\frac{U}{2}$, as discussed in section 1.1.5. We therefore expect the spectral function to be peaked at the Fermi energy $\omega = 0$ and impurity energy $\omega = \pm\frac{U}{2}$. We observe a similar feature in Fig. D.1 for $V = 0.09$, though we see unphysical oscillations for $V = 0.23$. At this stage of research we are unsure of the origin of this unphysical result.

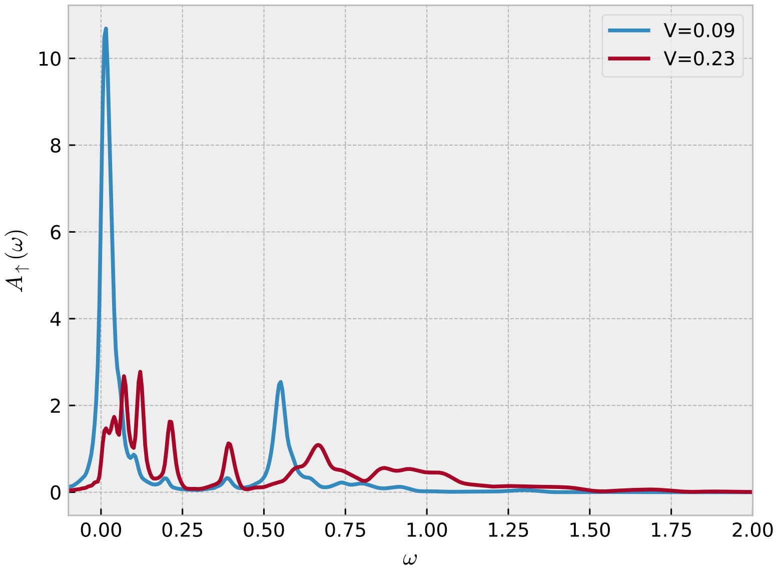

Figure D.1: Numerical results for the spectral function of the Anderson Impurity model with the KPM. The on-site energy is set to $\varepsilon_d = -\frac{U}{2}$ with the Coulomb interaction $U = 1$. The results were obtained for a chain length of 20 and a bond dimension of 40 with an energy resolution of 0.01.

Bibliography

[1] Richard P. Feynman. Simulating physics with computers. *International Journal of Theoretical Physics*, 21(6/7), 1982.

[2] Stephan W Koch et al. *Semiconductor quantum dots*, volume 2. World Scientific, 1993.

[3] H. D. Cheong Y. H. Jeong T. Hayashi, T. Fujisawa and Y. Hirayama. Coherent manipulation of electronic states in a double quantum dot. *Phys. Rev. Lett.*, 91(226804), 2003.

[4] D. G. Hasko J. Gorman and D. A. Williams. Charge-qubit operation of an isolated double quantum dot. *Phys. Rev. Lett.*, 95(090502), 2005.

[5] J. M. Taylor E. A. Laird A. Yacoby M. D. Lukin C. M. Marcus M. P. Hanson A. C. Gossard J. R. Petta, A. C. Johnson. Coherent manipulation of coupled electron spins in semiconductor quantum dots. *Science*, 309(5744), 2005.

[6] Jun Kondo. Resistance minimum in dilute magnetic alloys. *Progress of Theoretical Physics*, 32(1), 1964.

[7] B. Podolsky A. Einstein and N. Rosen. Can quantum-mechanical discription of physical reality be considered complete? *Physical Review*, 47(777), 1935.

[8] W. Heisenberg. Über quantentheoretische umdeutung kinematischer und mechanischer bezieungen. *Zeitschrift für Physik*, 33(1), 1925.

[9] E. Schrödinger. Quantisierung als eigenwertproblem. *Ann. Phys.*, 384(4), 1926.

[10] Fine-structure constant - nist. `https://physics.nist.gov/cgi-bin/cuu/Value?alphinv`. Accessed: 2018-09-27.

[11] Clemens Rössler Alexander Wolfertz Gianni Blatter Thomas Ihn Klaus Ensslin Christian Reichl Werner Wegschneider Giorgio Nicoli, Michael Sven Ferguson and Oded Zilberberg. Cavity-mediated coherent coupling between distant quantum dots. *Phys. Rev. Lett.*, 120(236801), 2018.

[12] T. Ihn K. Ensslin G. Blatter O. Zilberberg M. S. Ferguson, C. Rössler. Transport spectroscopy of singlet-triplet quantum dot states coupled to electronic cavities. *arXiv:1612.03850*, 2018.

[13] Clemens Rössler Thomas Ihn Klaus Ensslin Gianni Blatter Michael Sven Ferguson, David Oehri and Oded Zilberberg. Long-range spin-coherence in a strongly-coupled all electronic dot-cavity system. *Phys. Rev. B*, 96(235431), 2017.

[14] Edson Vernek Gerson J. Ferreira Luis G. G. V. Dias das Silva, Caio H. Lewenkopf and Sergio E. Ulloa. Conductance and kondo interference beyond proportional coupling. *Phys. Rev. Lett*, 119(116801), 2017.

[15] J. de Boer W. de Haas and G. van den Berg. The electrical resistance of gold, copper and lead at low temperatures. *Physica 1*, 1115, 1934.

[16] Ulrich Schollwöck. The density-matrix renormalization group in the age of matrix product states. *Annals of Physics*, 326(1), 2011.

[17] Thomas Pruschke Ralf Bulla, Theo A. Costi. The numerical renormalization group method for quantum impurity systems. *Rev. Mod. Phys.*, 80(395), 2008.

[18] Andreas Weichselbaum Hamed Saberi and Jan von Delft. Matrix-product-state comparison of the numerical renormalization group and the variational formulation of the density-matrix renormalization group. *Phys. Rev. B*, 78(035124), 2008.

[19] Andreas Alvermann Alexander Weiße, Gerhard Wellein and Holger Fehske. The kernel polynomial method. *Rev. Mod. Phys.*, 78(275), 2006.

[20] Ian P. McCulloch Ulrich Schollwöck Andreas Holzner, Andreas Weichselbaum and Jan von Delft. Chebyshev matrix product state approach for spectral functions. *Phys. Rev. B*, 83(195115), 2011.

[21] J. R. Schrieffer and P. A. Wolff. Relation between the anderson and kondo hamiltonians. *Physical Review*, 149(2), 1966.

[22] Kenneth G. Wilson. The renormalization group: Critical phenomena and the kondo problem. *Rev. Mod. Phys.*, 47(773), 1975.

[23] Peter W. Shor. Polynomial-time algorithms for prime factorization and discrete logarithms on a quantum computer. *SIAM J. COMPUT.*, 26(5), 1997.

[24] Daniel S. Abrams and Seth Lloyd. Simulation of many-body fermi systems on a universal qunantum computer. *Phys. Rev. Lett.*, 79(13), 1997.

[25] Thomas Ihn. *Semiconductor Nanostructures: Quantum states and electronic transport*. Oxford, 2009.

[26] B. L. Jones and J. W. McClure. Normal-fermi-liquid theory for electrons in solids. *Physical Review*, 143(1), 1966.

[27] P. W. Anderson. Localized magnetic states in metals. *Physical Review*, 124(1), 1961.

[28] Kenneth G. Wilson. Renormalization group methods. *Advances in Mathematics*, 16(170-186), 1975.

[29] H. Suhl. Dispersion theory of the kondo effect. *Physical Review*, 138(2A), 1965.

[30] R Bulla. Anderson impurity in pseudo-gap fermi system. *J. Phys.: Condens. Matter*, 9(10463), 1997.

[31] T. A. Costi R. Bulla and D. Vollhardt. Finite-temperature numerical renormalization group study of the mott transition. *Phys. Rev. B*, 64(045103), 2001.

[32] F. De Proft P. Geerlings and W. Langenaeker. Conceptual density functional theory. *Chem. Rev.*, 103(5), 2003.

[33] Dmitry Yu. Zubarev Brian M. Austin and William A. Lester Jr. Quantum monte carlo and related approaches. *Chem. Rev.*, 112(1), 2012.

[34] Matthias Troyer Giuseppe Carleo. Solving the quantum many-body problem with artificial neural networks. *Science*, 355(6325), 2017.

[35] M. Cramer J. Eisert and M. Plenio. Area laws of the entanglement entropy a review. *Rev. Mod. Phys.*, 82(277), 2010.

[36] Isaac L. Chuang Michael A. Nielsen. *Qunatum Computation and Quantum Information*. Cambridge, 2012.

[37] Thomas Köhler Sebastian Paeckel and Salvatore R. Manmana. Automated construction of u(1)-invariant matrix-product operators from graph representation. *SciPost Phys.*, 3(035), 2017.

[38] S. White. Density matrix formulation for quantum renormalization group. *Phys. Rev. Lett.*, 69, 1992.

[39] R.R. Schaller. Moore's law: past, present and future. *IEEE Spectrum*, 34(6), 1997.

[40] Matthias Troyer Sebastian Keller, Michele Dolfi and Markus Reiher. An efficient matrix product operator representation of the qunatum chemical hamiltonian. *The Journal of Chemical Physics*, 143(244118), 2015.

[41] J. W. Wilkins H. R. Krishna-murthy and K. G. Wilson. Renormalization-group approach to the anderson model of dilute magnetic alloys. i. static properties for the symmetric case. *Phys. Rev. B*, 21(3), 1980.

ETH
Eidgenössische Technische Hochschule Zürich
Swiss Federal Institute of Technology Zurich

Declaration of originality

The signed declaration of originality is a component of every semester paper, Bachelor's thesis, Master's thesis and any other degree paper undertaken during the course of studies, including the respective electronic versions.

Lecturers may also require a declaration of originality for other written papers compiled for their courses.

I hereby confirm that I am the sole author of the written work here enclosed and that I have compiled it in my own words. Parts excepted are corrections of form and content by the supervisor.

Title of work (in block letters):

KONDO PHYSICS WITH MATRIX PRODUCT STATES

Authored by (in block letters):
For papers written by groups the names of all authors are required.

Name(s):	**First name(s):**
Sack	Stefan Hermann

With my signature I confirm that
- I have committed none of the forms of plagiarism described in the 'Citation etiquette' information sheet.
- I have documented all methods, data and processes truthfully.
- I have not manipulated any data.
- I have mentioned all persons who were significant facilitators of the work.

I am aware that the work may be screened electronically for plagiarism.

Place, date	**Signature(s)**
Zürich, 27.9.18	

For papers written by groups the names of all authors are required. Their signatures collectively guarantee the entire content of the written paper.